

**UNIVERSALLY
POLARIZATION-INSENSITIVE
ACHROMATIC METASURFACES**

A THESIS SUBMITTED TO
THE GRADUATE SCHOOL OF ENGINEERING AND SCIENCE
OF BILKENT UNIVERSITY
IN PARTIAL FULFILLMENT OF THE REQUIREMENTS FOR
THE DEGREE OF
MASTER OF SCIENCE
IN
ELECTRICAL AND ELECTRONICS ENGINEERING

By
İbrahim Tanrıöver
July 2019

UNIVERSALLY POLARIZATION-INSENSITIVE ACHROMATIC
METASURFACES

By İbrahim Tanrıöver

July 2019

We certify that we have read this thesis and that in our opinion it is fully adequate,
in scope and in quality, as a thesis for the degree of Master of Science.

Hilmi Volkan Demir(Advisor)

Sergey Vasil'evich Gaponenko

Onur Tokel

Approved for the Graduate School of Engineering and Science:

Ezhan Kardeşan
Director of the Graduate School

ABSTRACT

UNIVERSALLY POLARIZATION-INSENSITIVE ACHROMATIC METASURFACES

İbrahim Tanrıöver

M.S. in Electrical and Electronics Engineering

Supervisor: Prof. Dr. Hilmi Volkan Demir

July 2019

Transparent optical components constitute the key elements of modern electro-optical systems including optical sensors, displays and imaging systems. The working principle of conventional transparent components rely on gradual phase accumulation. As a direct result of their working principle, these components suffer from fundamental limitations on size. Metasurfaces, enabling full wavefront engineering in subwavelength thicknesses, are promising candidates to replace conventional optics and overcome the size limitations. Early examples of this concept include plasmonic metasurfaces containing sub-wavelength metallic structures. However, these plasmonic structures cannot reach practically sufficient efficiency levels in transmission mode due to fundamental ohmic losses. This strongly motivates high-efficiency all-dielectric alternatives. These dielectric solutions have thus far been reported to rely on either the resonance tuning or the geometrical (Pancharatnam–Berry) phase. Though remedying the efficiency limitation, unfortunately, these approaches either are impaired with ultra-narrow operation bands or suffer polarization dependency. In this thesis, we propose and demonstrate two new approaches to address these problems. In the first approach of ours, universally polarization-insensitive achromatic wavefront control is achieved using dielectric nanopillars operated as step-index cylindrical waveguides intentionally away from the scattering resonances. A metalens operating in the mid-wave infrared region of electromagnetic spectrum is shown using these off-resonance waveguiding unit cells as a proof-of-concept demonstration. Polarization-insensitive diffraction-limited focusing over a broad spectral band of operation is verified by full electromagnetic simulations. In our second approach, to further increase the performance and bandwidth of dielectric metasurfaces, a novel architecture of these phase elements is proposed. Full phase control of wavefront is achieved using these unit cells. Such metalenses operating in

the mid-wave infrared and visible regions are designed as proof-of-concept demonstrations. Full electromagnetic solutions confirmed entirely polarization-insensitive achromatic focusing of the proposed metasurfaces with significantly increased operation bandwidth.

Keywords: Metasurfaces, waveguides, scatterers

ÖZET

EVRENSEL POLARİZASYON-BAĞIMSIZ AKROMATİK METAYÜZEYLER

İbrahim Tanrıöver

Electrical and Electronics Engineering, Yüksek Lisans

Tez Danışmanı: Prof. Dr. Hilmi Volkan Demir

Temmuz 2019

Şeffaf optik elemanlar, optik sensörler, ekranlar ve görüntüleme sistemleri gibi birçok modern elektro-optik sistemin anahtar bileşenlerini oluşturur. Geleneksel şeffaf optik elemanların çalışma prensibi faz biriktirmeye dayanır. Çalışma prensiplerinin doğrudan sonucu olarak, bu elemanlar belirli alt limitlerin altına inemez. Metayüzeyler, dalga boyundan küçük kalınlıklarda dalga yüzünün tam kontrolüne imkân sağladıkları için, geleneksel optik elemanların yerini alabilir ve onların maruz kaldığı boyut sınırlandırmalarını aşabilir. Metayüzey kavramının ilk örnekleri metal nanoyapılar kullanan plazmonik metayüzeylerdir. Ancak, plazmonik metayüzeyler temel optik kayıplara maruz kaldıkları için şeffaf optik parçalar olarak kullanıldıklarında düşük verimle çalışırlar. Bu durum araştırmacıları elektriksel olarak yalıtkan yapıları kullanmaya yönlendiriyor. Bu yalıtkan malzemelerin kullanıldığı çalışmalar şimdiye kadar genel olarak rezonans ayarlama ve Pancharatnam-Berry (PB) fazı, diğer adıyla geometrik faz, yaklaşımlarına dayanıyor. Verim üzerindeki kısıtlamaları aşmış olsalar da, bu çalışmalarda önerilen ve gösterilen metayüzeyler, ya polarizasyon-bağımlılığından ya da dar bant genişliğinden muzdariptir. Biz bu tezde bu problemlere çözüm olarak iki yeni yaklaşım öneriyoruz. Bu yaklaşımlarımızdan ilkinde, kasıtlı olarak rezonanslardan uzakta silindirik dalga kılavuzları olarak çalıştırılan nanosütunlar kullanılarak polarizasyon-bağımsız akromatik dalga yüzeyi kontrolü başarıldı. Yaklaşımın başarısını ispatlamak için orta kızılötesi bantta çalışan bir metalens tasarlandı. Geniş bir frekans bandında çalışan yüksek verimli polarizasyon-bağımsız odaklama elektromanyetik simülasyonlar aracılığıyla gösterildi. İkinci yaklaşımımızda, ulaşılan bant genişliğini daha da ileriye taşımak ve performansı artırmak için özgün bir mimaride faz elemanları önerildi. Bu faz elemanları kullanılarak dalga yüzeyinin tam faz kontrolü sağlandı. Örnek uygulama

ve yaklaşımın geçerliliğinin ispatı olarak birisi orta kızılötesinde diğeri görünür ışıktta çalışan iki adet metalens tasarlandı. Elektromanyetik simülasyonlara dayanarak, önerilen metayüzey ile polarizasyon-bağımsız akromatik odaklama bir kez daha, ama bu defa çok daha geniş frekans bantlarında ve daha yüksek performans değerlerine sahip olarak gösterildi.

Anahtar Sözcükler: Metayüzeyler, dalga kılavuzları, saçıcılar

Acknowledgement

I thank my supervisor Prof. Hilmi Volkan Demir for valuable contributions to this thesis work.

I want to thank Prof. Sergey V. Gaponenko and Asst. Prof. Onur Tokel for accepting to be in my thesis jury.

I would like to acknowledge TUBİTAK-BİDEB for the financial support.

I would like to thank past and present members of Demir Research Group and UNAM. In particular, I want to thank Dr. Murat Olutaş, Dr. Savaş Delikanlı, Dr. Yusuf Keleştemur, Dr. Kıvanç Güngör, Dr. Onur Akın, Onur Erdem, Nima Taghipour, Didem Dede, Selim Bozdoğan, Furkan Işık, Mustafa Sak and Esmâ Uçar for their trustworthy friendship.

Finally, I would like to thank my fiancé, Beria Keser, and family for their unconditional love and support.

Contents

1	Introduction	1
2	Background	4
2.1	The Resonance Tuning Approach	7
2.2	Pancharatnam-Berry Phase Approach	9
3	Mid-wave Infrared Broad-band Polarization-insensitive All-dielectric Metasurfaces	11
3.1	Narrow Operation Band and Polarization Dependency Problem	11
3.2	Off-resonance Waveguiding Approach	13
3.2.1	Step-index Cylindrical Waveguides	14
3.3	Modelling and Simulation	21
3.3.1	Metasurface Unit Cells	21
3.3.2	Metalens	26
3.4	Results and Discussion	27
3.5	Summary	34
4	Infrared and Visible Polarization-insensitive Achromatic All-dielectric Metasurfaces	35

4.1	Availability of High-index Material and Narrow Off-resonance Window Problem	35
4.2	Coupled Metasurfaces Approach	36
4.2.1	Coupled Scatterers	37
4.2.1.1	Linear Packing Scheme	38
4.2.1.2	Square Packing Scheme	42
4.2.1.3	Hexagonal Packing Scheme	43
4.3	Generality of Approach	44
4.4	Results and Discussion	46
4.4.1	Metalens at Infrared Region	46
4.4.2	Metalens at Visible Region	47
5	Conclusion.....	49
	Bibliography	51

List of Figures

Figure 2.1: Figure 2.1 Phase and amplitude response of an exemplary optical resonator Reprinted (or Adopted) with permission from [1].	8
Figure 3.1: A representative radial refractive index profile of a step-index cylindrical waveguide.....	14
Figure 3.2: Graphical demonstration of the solution for the HE modes.	16
Figure 3.3: Effective index variation of a step-index cylindrical waveguide.	17
Figure 3.4: Effective index difference between arbitrary waveguides across our spectral band of operation. Reprinted (or Adopted) with permission from [1].	18
Figure 3.5: Transmission and phase response of a step-index cylindrical waveguide with a radius of $R=440$ nm operating in the off-resonance regime. Reprinted (or Adopted) with permission from [1].	19
Figure 3.6: Transmission and phase response of a step-index cylindrical waveguide with a radius of $R=700$ nm operating in the on-resonance regime. Reprinted (or Adopted) with permission from [1].....	20
Figure 3.7: Side view of a unit cell. Reprinted (or Adopted) with permission from [1]	22

Figure 3.8: Electric field amplitude of the sample unit cell. Reprinted (or Adopted) with permission from [1].....	23
Figure 3.9: Comparison of the phase responses obtained from the FDTD simulations and the cylindrical waveguide solutions for our unit cell library.....	24
Figure 3.10: Phase response of the nanopillar unit cells as a function of the operating wavelength and the radius. Reprinted (or Adopted) with permission from [1]..	25
Figure 3.11: Transmission of the nanopillar unit cells as a function of the operating wavelength and the radius. Reprinted (or Adopted) with permission from [1]..	25
Figure 3.12: Top view of the lens with a 35 μm radius. Reprinted (or Adopted) with permission from [1].....	26
Figure 3.13: Field intensity at $y=0$ (xz) plane.....	27
Figure 3.14: Field intensity along the optical axis at the design wavelength (4.2 μm) and the borders of the spectral band of operation (4.2 μm and 4.6 μm).	28
Figure 3.15: Light distribution at the focal plane ($z=48$ μm plane) of metalens under 4.2 μm TM polarized light. Reprinted (or Adopted) with permission from [1].....	29
Figure 3.16: Light distribution at the focal plane ($z=48$ μm plane) of metalens under 4.2 μm TE polarized light. Reprinted (or Adopted) with permission from [1].....	29
Figure 3.17: Horizontal cut of the focal spot under TE and TM illumination. Reprinted (or Adopted) with permission from [1].	30
Figure 3.18: Horizontal cuts of the focal plane under illumination at 4.00, 4.15, 4.30, 4.45 and 4.60 μm . Reprinted (or Adopted) with permission from [1].	31
Figure 3.19: Focal distances of the metalens in the spectral band of operation. Reprinted (or Adopted) with permission from [1].	31

Figure 3.20: Relative and absolute efficiencies of the metalens in the spectral band of operation. Reprinted (or Adopted) with permission from [1].....	32
Figure 4.1 Electric field distribution over $z=1 \mu\text{m}$ plane of linearly packed scatterers under x -polarized illumination.	38
Figure 4.2: Phase response of medium (linearly packed scatterers under x -polarized illumination) versus gap between scatterers with respect to different scatterer radii.	39
Figure 4.3: Electric field distribution over $z=1 \mu\text{m}$ plane of linearly packed scatterers under y -polarized illumination.	40
Figure 4.4: Phase response of medium (linearly packed scatterers under y -polarized illumination) versus gap between scatterers with respect to different scatterer radii.	41
Figure 4.5: Electric field distribution over $z=1 \mu\text{m}$ plane of square packed scatterers under x -polarized illumination.	42
Figure 4.6: Phase response of medium (square packed scatterers) versus gap between scatterers with respect to different scatterer radii.	42
Figure 4.7: Electric field distribution over $z=1 \mu\text{m}$ plane of hexagonally packed scatterers.....	43
Figure 4.8: Phase response of medium (hexagonally packed scatterers) versus gap between scatterers under x (TM) and y (TE) polarized illumination.....	44
Figure 4.9: Transmission and phase responses of hexagonally packed silicon nanopillars at $3.2 \mu\text{m}$ wavelength and titanium oxide nanopillars at 550 nm wavelength.....	45

Figure 4.10: Transmission response of hexagonally packed a) silicon and b) silicon-aluminum oxide (optimized) pillars with various gap values.	45
Figure 4.11: Schematic of transmission optimized nanopillars.	46
Figure 4.12: Focal plane and its horizontal cut for the metalens working in the infrared region. The operation wavelength is 3.2 μm	46
Figure 4.13: a) Horizontal cut of the focal plane of lens. The full-width-half-maximum is $\sim 0.5 \mu\text{m}$. b) Focal length of lens along the visible spectrum. c) Relative and d) absolute focusing efficiencies of lens along the visible spectrum..	48

List of Tables

Table 3.1: Performance metrics of previously reported metalenses and comparison to this work. Reprinted (or Adopted) with permission from [1].	32
Table 3.2: Figure of merits (FoMs) defined to quantitatively analyze broad-band performance. Reprinted (or Adopted) with permission from [1].	33
Table 3.3: Comparison of previous reports and this work in terms of the defined FoMs. Reprinted (or Adopted) with permission from [1].	34
Table 4.1: Scaling parameters of scatterers.....	44
Table 4.2: Performance of Coupled Metalens.....	47

Chapter 1

Introduction

Light is essential for vision, which is one of the most important abilities of humankind. Owing to its importance, understanding and controlling light have been among the strongest endeavours of humankind throughout the history. The effort put to understand and manipulate light led to the birth of the field of optics. The field of optics has its roots back to ancient Egypt and Mesopotamia. Assyrians made the earliest known lenses by polishing quartz [1]. Ancient Greeks filled glass spheres with water to bend and focus the light. Philosophers of ancient Greece, Rome and Islamic world developed several optical components including prisms, mirrors and lenses, and proposed theories to explain the nature of light. After the renaissance, pioneer scientists including Kepler, Newton and Huygens developed new, complex optical components, and improved our understanding of light. Then, Young's and Fresnel's studies on the interference of light gave birth to the wave optics. The wave approach was unified by Maxwell's electromagnetic theory. These developments were followed by the studies of famous physicists, Einstein and Planck. Their work revealed the particle nature of light, and as a result, today our understanding of light depends on the wave-particle duality.

The effort put forth in the field of optics also bring results in terms of enabling technological development. For example, following the first glasses invented in the 13th century, Galileo made telescopes to observe the universe. After the discovery of electricity

and later the solid state devices, electronics was integrated to optics, and electro-optical systems were born. Today's imaging systems, displays, and optical sensors are among the examples of such electro-optical systems. These systems are composed of optical component and electronic circuitry. Today, electronic part has the capability to operate at a high speed and has been shrunk to sub-micron to several nanometers, in size. However, despite their long history of development, conventional optical components, typically several micrometres to centimetres in size, still suffer from fundamental limitations on the size and performance.

The working principle of conventional transparent optical components is based on the gradual phase accumulation that occurs as the light travels inside the medium. As a well-known fact, the accumulated phase is directly proportional to refractive index of the medium and the distance travelled by light, and inversely proportional with the wavelength of light. Based on this gradual phase accumulation, conventional optical components achieve many functionalities by controlling the shape of wavefront and polarization state of light. It is therefore possible to achieve full control over phase and polarization states of light by using materials as long as they have the required refractive index. On the other hand, the materials that are transparent in the visible and/or mid-wave infrared (MWIR) region is limited, and their refractive indices covers narrow range approximately from 1.4 to 4.2. As a result, this strong dependency of the gradual phase accumulation on the material refractive index restricts optical functionalities feasible with conventional optical components. Certain functionalities require conventional optical components to be thick and bulky. And, some functionalities are not even achievable with gradual phase accumulation approach due to the aforementioned limited refractive index range of transparent materials.

As an attempt to overcome the limitations that are aroused from the narrow range of accessible refractive indices in the nature, the concept of metamaterials has been introduced. Based on this concept, refractive indices that are effectively too large, too small (close to zero) or even negative have been achieved, and various novel phenomena including negative refraction, cloaking and sub-wavelength resolution [2-5]. In spite of these promising achievements, metamaterials still suffer from certain drawbacks. For

example, metals are used to obtain abnormal effective refractive index values, and they introduce fundamental optical losses. Metamaterials are also still relatively thick, which can diminish their performance [6].

In the past few years, the concept of flat optics using metasurfaces has also emerged as one of the strongest candidates enabled by surface patterning (rather than the volume) of a medium to take place of conventional optical components. Unlike the conventional optics, the operating principle of metasurfaces does not depend on the propagation of light inside the medium. The concept is based on introducing abrupt changes on phase, amplitude and polarization state of light over a surface with sub and near-wavelength resolutions [7]. Metasurfaces consist of spatially arranged arrays of nano- and/or microstructures. These structures have sub and near-wavelength dimensions on both horizontal and vertical directions. They work as scatterers, waveguides and/or antennas. As such, the aforementioned abrupt changes stem from the interaction between light and these structures. The subwavelength thicknesses of metasurfaces enable us to overcome the size limitations otherwise faced in various applications including wearable and portable devices [8] in the case of using bulky optics. To date, many optical components, such as polarizers, beam splitters, holograms and lenses [9-31], have been realized based on this concept. Initial examples of metasurfaces were the plasmonic ones that use metallic nanostructures as optical scatterers and antennas [18,21,22]. Although these plasmonic metasurfaces constitute very successful examples in terms of wavefront control, they suffer from fundamental Ohmic losses [21]. As a result, they were limited in efficiency in the transmissive mode.

The low efficiencies of plasmonic metasurfaces guided researchers through all-dielectric solutions. As the building blocks of dielectric metasurfaces do not introduce absorption losses, the only source of optical loss is the reflection. And, avoiding reflection as much as possible is an important part of the design. As a result, all-dielectric metasurfaces can achieve significantly higher efficiencies in the transmissive mode [9-17,19,20,23-25,27-31]. The working principle of these high efficiency all-dielectric metasurfaces depends on two main approaches. First of them is the resonance tuning approach [20,23,29,30]. This approach is based on the interaction of light with sub-

wavelength nanostructures in the resonant scattering regime. These resonances cause abrupt changes in both phase and transmission response of the nanostructures, which act as resonators. By combining relative phase responses of different resonators, a unit cell library, which covers phase change of 0 to 2π , is obtained. These resonators can be designed to exhibit cylindrical and/or cartesian symmetry. As a result, their phase and transmission responses become identical for two perpendicular polarizations of light, either circular or linear. Since any polarization state can be expressed as a linear combination of two perpendicular polarizations, their symmetry makes them polarization-insensitive, which is a desired property for certain applications.

Despite their favourable property of polarization insensitivity in the case of symmetric structures, all-dielectric metasurfaces based on the resonance tuning approach also have a significant drawback. Their operation is limited to narrow spectral bands of their resonant scattering regime. Several attempts have been made to overcome this significant limitation. For example, some multi-wavelength design proposed [15]. However, these designs work only for specific wavelengths. They do not provide us with the desired broad-band operation.

The second approach is based on the geometric phase, also known as Pancharatnam-Berry (PB) phase [11,12,16–18,31]. In this approach, the phase response depends on adiabatic change of the polarization state of light. Different than the resonance tuning approach, metasurfaces operating along broad-spectral bands have been shown using PB phase [16-18,31]. However, this approach is highly polarization dependent. The metasurfaces utilizing geometric phase approach can work only under circularly polarized illumination, and this severely limits their functionality. As a result, literature lacks a polarization-insensitive all-dielectric solution operating at broad-spectral bands.

In this thesis work, to address the need for polarization-insensitive broad-band operation, we proposed and demonstrated two novel approaches, which we name the off-resonance waveguiding and coupled metasurface approaches. Based on our approaches, we designed sub-wavelength structures as metasurface building blocks. We modelled, simulated and optimized them to provide desired phase and transmission responses. Then, we demonstrated several optical components, which operate in the visible and MWIR

ranges as proof-of-concept examples. The performance of these optical components are compared with previous examples from literature. And, their advantages and disadvantages over existing approaches were discussed. Furthermore, we explained in detail the physical mechanisms behind these proposed approaches including how we actually model them and which assumptions were made. For all these steps, we present our simulation results and calculations.

The remaining part of this thesis contains 5 chapters. In Chapter 2, we introduce the metasurface phase elements. We start our discussion by providing some background information. This part includes brief review of existing approaches in the literature, which are the resonance tuning and Pancharatnam-Bery phase approaches. Governing physics behind these approaches is also explained along with brief discussions on their advantages and disadvantages.

In Chapter 3, our off-resonance waveguiding approach is introduced to address both narrow operation band and polarization dependency problems. Cylindrical step index waveguides, which are the phase elements of the off-resonance waveguiding approach, are explained. Maxwell equations are solved for the fundamental mode supported by these waveguides. Their operation over broad spectral bands in the on- and off-resonance regimes are discussed. A library of unit cells and focusing metalens, which is made of this unit cell library, are designed using Lumerical FDTD solver. Modelling and simulations of both the unit cells and the metalens are explained as well. Finally, the performance of the metalens is compared with previously reported examples from the literature.

In Chapter 4, our coupled metasurface approach is introduced. The improvements offered by this approach are discussed. Operation of coupled scatterers, which are the phase elements of this approach, is explained for two perpendicularly polarized incidence. Then, their general working principle is explained. Their operation under different packing schemes and the effect of geometric parameters on their relative phase response are discussed. Generality of our approach is shown and two metalenses that operate in different spectral bands are designed as a proof-of-concept demonstration. At the end of this chapter, the performance of these metalenses is discussed.

In Chapter 6, this thesis is concluded by summarizing key points.

Chapter 2

Background

Sub-wavelength dielectric disks [14], cylindrical pillars [1,10], square and/or rectangular blocks [11], and plasmonic nanoantennas [21, 32-49] can be used as metasurface phase elements. Plasmonic nanoantennas constitute the initial examples of metasurfaces because of their tailorable optical responses and ease of fabrication. However, plasmonic nanoantennas are limited in efficiency in the transmissive mode since they suffer from fundamental Ohmic losses. This efficiency problem motivated researchers to investigate all-dielectric solutions.

All-dielectric metasurfaces were designed to achieve high transmission efficiencies, where the materials used are highly transparent [9–17,19,20,23–25,27–31]. These metasurfaces can be divided into two broad classes as the ones based on the resonance tuning approach [20,23,28,30] and the ones based on Pancharatnam-Berry (PB) phase [11,12,16–18,31]. Although many optical functionalities were realized based on these approaches, they suffer from different fundamental limitations. The former class of metasurfaces are generally polarization-insensitive but their operation is limited to narrow spectral bands. The latter class can operate across broad spectral bands but they suffer

from their dependency on circularly polarized illumination. To address these limitations, we proposed two novel classes of metasurfaces, which will be discussed in later chapters.

This chapter contains two sections. In the first section, we discuss the resonance tuning approach and provide some background information. In Section 2, general working principle of PB phase is briefly explained. In this section, some background is also provided with a brief discussion on the performance of the latest examples from literature.

2.1 The Resonance Tuning Approach

Resonance tuning approach is one of the main techniques to design metasurface phase elements. This approach enables us to design polarization-insensitive phase elements and, as a result, polarization-insensitive metasurfaces. However, metasurfaces that rely on this method suffer from very limited operation bandwidths.

Resonance tuning approach relies on the phase shifts introduced by subwavelength scatterers, which act as optical resonators. These optical resonators are working in or near the resonant scattering regime in order to cover the phase change range of 0 to 2π , which is essential to obtain full phase control over the wavefront. Despite the plasmonic resonators, which can only cover 0 to π range, dielectric resonator can cover the entire 0 to 2π range as they support both magnetic and electric dipolar modes [8].

At resonance, the phase and amplitude response of the scatterer exhibits sudden jumps, as seen in figure 2.1. The strength of the jumps depends on the strength of resonance or, in other words the quality (Q) factor of the resonator. The spectral position of these jumps depend on the size of the scattering element. This size-dependent resonance frequency enables us to control and tune the position of resonances by changing the dimensions of the scatterer. These resonances can be tailored to obtain a unit cell library covering the entire 0 to 2π range. This tailoring is realized by designing resonators, which are operating at slightly different spectral positions. The polarization of scattered light is the same with the polarization of incident light. As a result, these scatterer are polarization-insensitive, as long as they separately provide the same phase response for two perpendicularly

polarized incidence. This requirement can be easily satisfied by designing scatterers that have a least two perpendicular symmetry axes. Nanosquares [29] and nanodisks [14,20,23,30] are the most common examples.

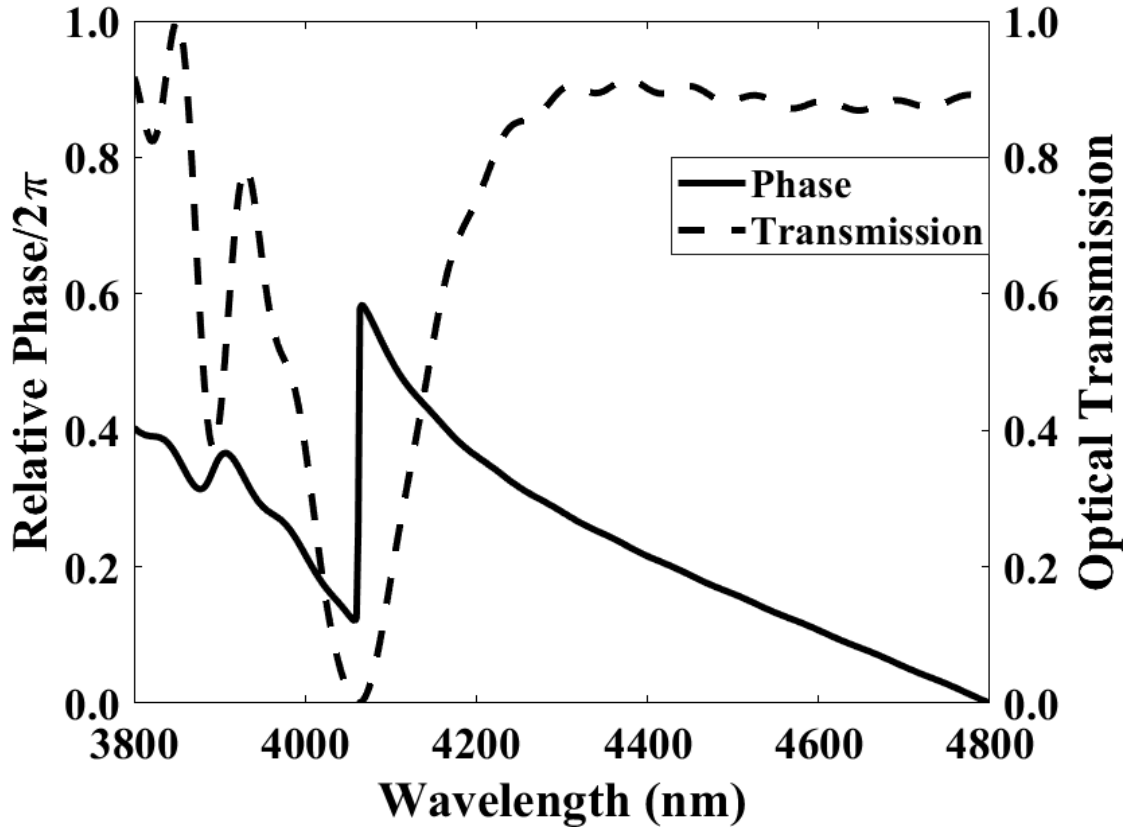


Figure 2.1 Phase and amplitude response of an exemplary optical resonator, which is made of a Si nanopillar with a radius of 700 nm and a height of 2 μm placed on top of a quartz (SiO_2) substrate. The dashed line is the optical transmission and the solid line is the phase response of the pillar. The dips in the transmission line at around 3,900 nm and 4,070 nm wavelengths correspond to the optical resonances, where apparent jumps occur at the corresponding phase response. Reprinted (or Adopted) with permission from [53]. Copyright 2019 American Institute of Physics.

The main drawback of the resonance tuning approach is the narrow operation bands. As mentioned, the operation principle of resonant scatterers relies on the phase jumps occurring at the resonance points. These jumps are spectrally narrow as the resonances

and lose their effects on the phase response beyond a short spectral range. As a result, the approach itself limits its operation bandwidth by relying on these restricted phase responses. Another drawback of the resonance tuning approach also stems from using the resonances. As mentioned above, the 2π coverage is essential for full wavefront control but there is also another condition to satisfy. Since the resulting wavefront is formed as the result of collective interference of scattered light from unit cells, the amplitude response of the unit cells should be equal, in ideal case, to provide completely destructive and/or constructive interferences. However, at resonances, the amplitude responses of optical resonators exhibit sudden dips and peaks, as seen from figure 2.1. Note that the width of these peaks and dips depend on the Q-factor of the resonator. These abrupt changes create a great difference between the amplitudes of light that are to be interfere. As a result, the interference efficiency decreases drastically. This limits the device performance not only in terms of the efficiency but also in terms of the quality. For example, the width of a focal spot from a converging lens would increase and light rings will start to appear around the focal spot as the difference between the amplitude responses of unit cells increases.

2.2 Pancharatnam-Berry Phase Approach

Pancharatnam-Berry (PB) phase is also known as geometric phase. Geometric phase corresponds to the phase difference that is acquired when a system is subjected to a cyclic adiabatic process in classical and quantum mechanics. In optics, and thus in metasurface design, this adiabatic process is polarization conversion [50].

This phenomenon has been experimentally demonstrated by Pancharatnam [Pancharatnam]. Later, Berry generalized the theory using quantum mechanics [51]. He also made a very important discovery in the phenomenon. The polarization change does not have to be slow. Instantaneous changes also result in the desired phase shift. This idea has led researchers to use PB phase as a convenient approach to design metasurface phase elements [11,12,16-18,31].

This is an off-resonance approach. Therefore, the phase responses can be considered as steady-state solutions. As a result, the metasurfaces designed relying on this approach

have wide operation bandwidths, in contrary to the ones depending on the resonance tuning approach. However, the metasurfaces depending on PB phase are polarization-dependent as the phase shift mechanism depends on the polarization conversion [8,11,12,16-18,21,31]. They provide desired functionality only under circularly polarized illumination. Some metasurfaces have been designed in the near past, which were polarization-insensitive, using coupled anisotropic nanofins and PB phase approach [52]. However, these approaches use PB phase only to extend the phase coverage range of anisotropic nanofins from π to 2π , and as an additional drawback, this metasurface suffers from very low efficiencies.

Chapter 3

Mid-wave Infrared Broad-band Polarization-insensitive All-dielectric Metasurfaces

This chapter is based on the publication “Broad-band polarization-insensitive all-dielectric metalens enabled by intentional off-resonance waveguiding at mid-wave infrared” **I. Tanriover** and H.V. Demir, Appl. Phys. Lett. 114, 043105 (2019) [53]. Adapted (or “Reproduced in part”) with permission from American Institute of Physics. Copyright 2019 American Institute of Physics.

3.1 Narrow Operation Band and Polarization Dependency Problem

Pioneering examples of metasurface concept have used metallic structures, which act as plasmonic nanoantennas. Various optical phenomena have been realized and many optical components have been designed using these plasmonic metasurfaces. However, their limited efficiencies constitute a significant disadvantage for them to take place of commercial transmissive optical components. This fundamental disadvantage has led

researchers towards all-dielectric solutions. All-dielectric metasurfaces can be divided into two main classes as the ones that are based on the resonance tuning approach, and the ones that are based on PB phase. The former class of metasurfaces provide polarization-insensitive operation, whereas they are limited to narrow operation bands. Although the latter class can exhibit broadband operation, they are strictly dependent on circularly polarized illumination, as discussed in Chapter 2. As a result, a class of metasurfaces providing broad-band operation under arbitrarily polarized incidence still lacks to date.

Polarization dependency introduces an important limitation over the commercial usage of metasurfaces. Although certain applications, such as laser-based spectroscopy, use polarized light, many real-life applications including imaging, sensing and displays are based on unpolarized light sources. This problem can be solved by altering the polarization state of light. However, this is not a feasible solution as it brings new problems with it. First, alignment problems arise since this solution requires additional optical components, such as wave plates. With the addition of other optical components, size and cost of the system also increase. Additionally, altering the polarization state of unpolarized light means allowing only certain polarizations and blocking others. This, in turn, brings about large optical losses even with perfect polarizers. When the arising problem of alignment, size, cost and efficiency problems are taken into account, polarization-sensitive metasurfaces lose their advantages over commercial optical components for the applications that are based on unpolarized incidence.

Many real-life applications including both consumer and industry products require broadband operation. Imaging is a well-known example. For imaging, all optical components should maintain constant performance across the whole visible spectrum. For example, focal length, focal spot full-width-half-maximum (FWHM) and transmission level of a converging lens should be constant to ensure achromatic imaging. When these characteristics change with wavelength or the lens does not operate properly in some portions of the targeted spectrum, distortions occurs on the image. These distortions are known as chromatic aberrations. Chromatic aberrations decrease resolution. As indicated with this example, the operation bandwidth is an important performance metric that cannot

be compromised. As a result, there is a strong need for a new approach to simultaneously address both the polarization sensitivity and limited operation band problems.

3.2 Off-resonance Waveguiding Approach

To achieve polarization-insensitivity across a wide spectral band of operation, we propose a novel approach that relies on using step-index waveguides operated as metasurface phase elements. These waveguides are intentionally designed to operate in the off-resonance regime. Adopting cylindrical step-index waveguides as the elemental units, polarization-insensitivity is ensured as a result of the circular symmetry of these waveguides. Here the main phase shift mechanism depends on waveguiding. As a supported optical mode propagates inside a waveguide element, it experiences a certain level of phase delay and thus feels an effective refractive index. This effective refractive index depends on the various characteristics of the waveguide including geometrical parameters and optical properties of materials the waveguide is made of. In our case, we use the same material to design all waveguides, and the only variable that is tuned is the radius of our cylindrical step-index waveguides once their height is set to a reasonable value. As a result, the effective index differences between our waveguides are radius-dependent. This, in turn, creates a radius-dependent phase accumulation difference between the waveguide elements as the accumulated phase is directly proportional to the effective index of medium. The other critical aspect of our approach is to deliberately operate in the off-resonance regime. The resonances prevent broadband operation by disturbing optical responses of waveguides. Here, avoiding resonances, such disruptions of the targeted wide-spectrum operation is prevented.

In this section, the governing physical phenomena of our approach are explained in detail. We solved Maxwell's equations for the proposed step-index cylindrical waveguide elements of varying radii. We calculated cut-off values, propagation constants and effective indices for guided modes in these waveguides. Based on these solutions, their operation across wide spectral bands is obtained. Then, we compared our results using finite difference time domain (FDTD) simulations, which were conducted using a

commercial software, Lumerical Inc. FDTD Solutions. With the knowledge that we have gained from this comparison, effects of the resonances on the phase and transmission response of cylindrical waveguides were further explored. Taking into account all of these results, our approach has reached its final and complete form.

3.2.1 Step-index Cylindrical Waveguides

A step-index cylindrical waveguide consists of a circular center (called core) and a surrounding ring (called cladding). Its radial refractive index profile is shown in Figure 3.1. As seen in the Figure, the refractive index of core, n_{core} , is larger than the refractive index of the cladding, $n_{cladding}$. During calculations, we assumed that the radius of cladding, r_2 , is large enough so that the fields of confined modes decay to zero at $r = r_2$. Based on this assumption, we take $r_2 = \infty$. For confined mode calculations of uncoupled waveguides, this assumption is legitimate [54].

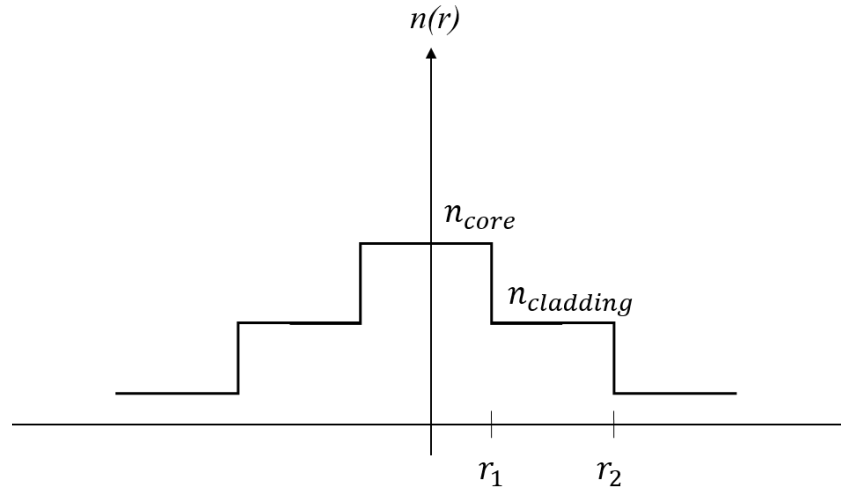


Figure 3.1 A representative radial refractive index profile of a step-index cylindrical waveguide.

We are interested in the solution of confined modes. The confined modes of circular waveguides are mixtures of TE and TM modes. These hybrid modes are denoted as HE and EH modes. These modes satisfy the condition; $n_{cladding}k_0 < \beta < n_{core}k_0$, where β is the propagation constant of a confined mode and k_0 is the free space propagation

constant. The resulting fields are evanescent in the cladding ($r > r_2$). The core and cladding fields are given as follows [54]:

$$E_z(r, t) = AJ_l(hr)e^{j(\omega t + l\phi - \beta z)} \quad (3.1)$$

$$H_z(r, t) = BJ_l(hr)e^{j(\omega t + l\phi - \beta z)}$$

and

$$E_z(r, t) = CK_l(qr)e^{j(\omega t + l\phi - \beta z)} \quad (3.2)$$

$$H_z(r, t) = DK_l(qr)e^{j(\omega t + l\phi - \beta z)}$$

respectively, where $q = \beta^2 - n_{cladding}^2 k_0^2$ and $h = n_{core}^2 k_0^2 - \beta^2$. J_l is Bessel function of the first kind and K_l is modified Bessel function of the second kind. Solving azimuthal and radial components of electric and magnetic fields in terms of E_z and H_z , and applying the boundary conditions that the E_z , E_ϕ , H_z , and H_ϕ are continuous at the core-clad interface lead to the following mode condition:

$$\left(\frac{J'_l(hr)}{hrJ_l(hr)} + \frac{K'_l(qr)}{qrK_l(qr)} \right) \left(\frac{n_{core}^2 J'_l(hr)}{hrJ_l(hr)} + \frac{n_{cladding}^2 K'_l(qr)}{qrK_l(qr)} \right) = \frac{l^2}{n_{core}^2} \left[\left(\frac{1}{qr} \right)^2 + \left(\frac{1}{hr} \right)^2 \right]^2 \left(\frac{\beta}{k_0} \right)^2 \quad (3.3)$$

Applying the Bessel function relations

$$J_{l-1}(x) = \frac{l}{x} J_l(x) + J'_l(x) \quad (3.4)$$

$$J_{l+1}(x) = \frac{l}{x} J_l(x) - J'_l(x)$$

into Equation (3.3) follows

$$\frac{J'_{l-1}(hr)}{hrJ_l(hr)} = \left[\left(\frac{1}{hr} \right)^2 - R \right] - \left(\frac{K'_l(qr)}{qrK_l(qr)} \right) \left(\frac{n_{core}^2 + n_{cladding}^2}{2n_{core}^2} \right) \quad (3.5)$$

and

$$\frac{J'_{l+1}(hr)}{hrJ_l(hr)} = \left[\left(\frac{1}{hr} \right)^2 - R \right] + \left(\frac{K'_l(qr)}{qrK_l(qr)} \right) \left(\frac{n_{core}^2 + n_{cladding}^2}{2n_{core}^2} \right) \quad (3.6)$$

where

$$R = \left[\left(\frac{K'_l(qr)}{qrK_l(qr)} \right)^2 \left(\frac{n_{core}^2 - n_{cladding}^2}{2n_{core}^2} \right)^2 + \frac{l^2}{n_{core}^2} \left[\left(\frac{1}{qr} \right)^2 + \left(\frac{1}{hr} \right)^2 \right]^2 \left(\frac{\beta}{k_0} \right)^2 \right]^{1/2} \quad (3.7)$$

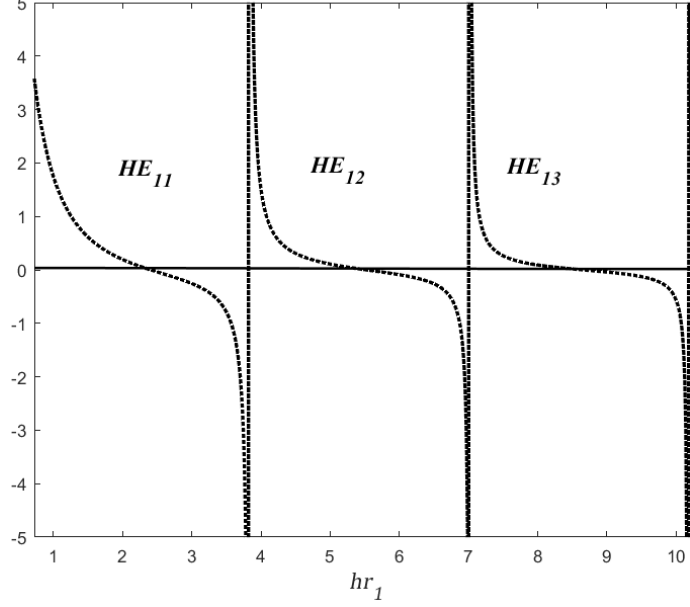


Figure 3.2 Graphical demonstration of the solution for the HE modes, where the dotted curve is the right-hand side and the solid line is the left-hand side of Equation (3.5). The x axis is hr_1 .

To find the propagation constants for HE and EH modes, Equations (3.5) and (3.6) are graphically solved, respectively. Figure 3.2 demonstrates an example solution for Equation (3.5), where the core of the waveguide is silicon ($n_{core} \cong 3.43$ [55]), the cladding is air ($n_{cladding} = 1$) and the core radius, r_1 , is $3 \mu\text{m}$. The equation was solved using MATLAB. For Bessel function of the first kind (J_l) and modified Bessel function of the second kind (K_l), we used MATLAB's built-in *besselj* and *besselk* functions. The propagation constant, β , of each mode was determined from the intersecting points.

For convenience, we designed our waveguides to support only the fundamental mode. The fundamental mode of a step-index cylindrical waveguide is HE_{11} mode, which does not have a cut-off value. From the propagation constants determined from Equation (3.5), we

calculated effective index values. The effective index, n_{eff} , of a step-index cylindrical waveguide is wavelength-dependent, and takes a value between the refractive indices of core and cladding, as illustrated in Figure 3.3.

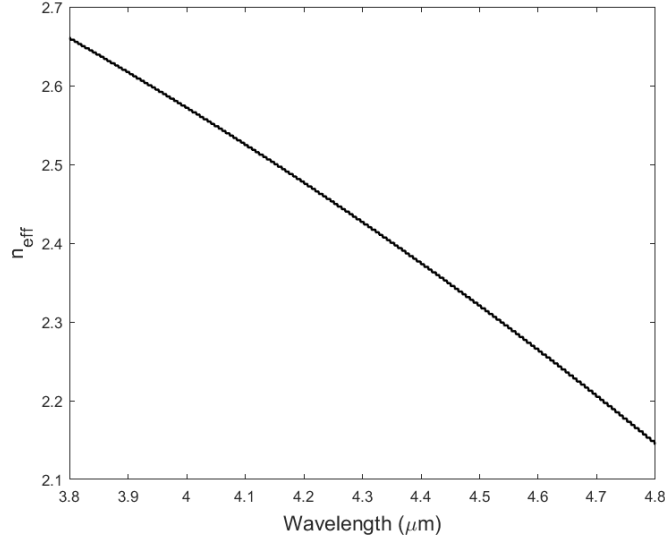


Figure 3.3 Effective index variation of a step-index cylindrical waveguide, which supports only the fundamental mode HE_{11} , with respect to the wavelength of operation. Here, the core is silicon, the cladding is air and the core radius is 600 nm.

The phase response of a waveguide is calculated as

$$\phi_{WG} = \frac{2\pi}{\lambda} n_{eff}(R, \lambda, n_{cladding}, n_{core})H \quad (3.8)$$

where H is the height of the waveguide, R is the radius of the core and λ is the operation wavelength.

In metasurface-based wavefront engineering, controlling the relative phase response of the unit cells across a full 2π range is the critical point of interest (while also maintaining a high-level of transmission or reflection in amplitude at a nearly fixed value). For instance, to make a focusing flat lens, the phase response that should be introduced by each phase element, which is a step-index cylindrical waveguide in our case, is

$$\phi_{req}(r) = -\frac{2\pi}{\lambda} (\sqrt{r^2 + f^2} - f) \quad (3.9)$$

where f is the focal length, λ is the wavelength, and r is the distance from the center. Equating Equations (3.8) and (3.9) for two arbitrary waveguides on a flat lens leads to

$$-(\sqrt{r_1^2 + f^2} - \sqrt{r_2^2 + f^2}) = h\Delta n_{eff}(R_1, R_2, \lambda) \quad (3.10)$$

where $\Delta n_{eff}(R_1, R_2, \lambda) = n_{eff}(R_1, \lambda) - n_{eff}(R_2, \lambda)$, r_1 and r_2 are the locations, and R_1 and R_2 are the radii of the two arbitrary waveguides. As the left-hand side of Equation (3.10) is constant, the right-hand side must also be constant over the targeted spectral range to secure perfectly achromatic operation. Figure 3.4 shows Δn_{eff} with respect to the wavelength of operation for arbitrary step-index cylindrical waveguides. As seen from the figure, Δn_{eff} is constant across the targeted spectral band of operation for each waveguide pair proving that the cylindrical waveguides satisfy this condition of the broad-band operation.

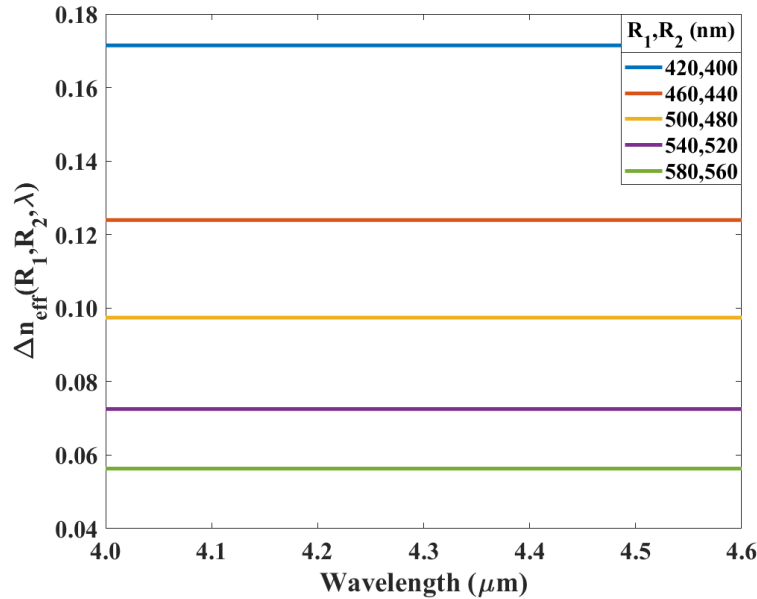


Figure 3.4 Effective index difference between arbitrary waveguides across our spectral band of operation. Reprinted (or Adopted) with permission from [53]. Copyright 2019 American Institute of Physics.

The calculations made to this point proves that step-index cylindrical waveguides may provide broad-band operation. However, note that the coupling of incident light into waveguides and finite length of these waveguides are not included in these calculations. As a result, scattering of the incident light has not been taken into account up to this point.

To further calculate the effect of scattering and other optical phenomenon on the phase response of our waveguides, we conducted FDTD simulations using the commercial program (Lumerical Inc. FDTD Solutions). Transmission and phase responses of these waveguides were obtained from these simulations. The phase responses calculated using the waveguide calculations and those obtained from FDTD our simulations were compared. Figures 3.5 and 3.6 show the comparison of the simulation and calculation results for the off-resonance and the on-resonance cases, respectively.

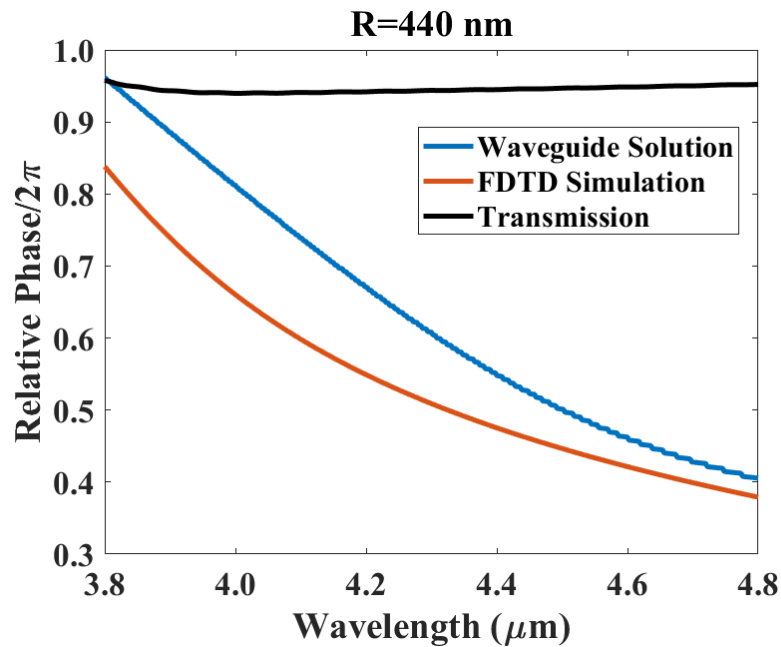


Figure 3.5 Transmission and phase response of a step-index cylindrical waveguide with a radius of $R=440$ nm operating in the off-resonance regime. Reprinted (or Adopted) with permission from [53]. Copyright 2019 American Institute of Physics.

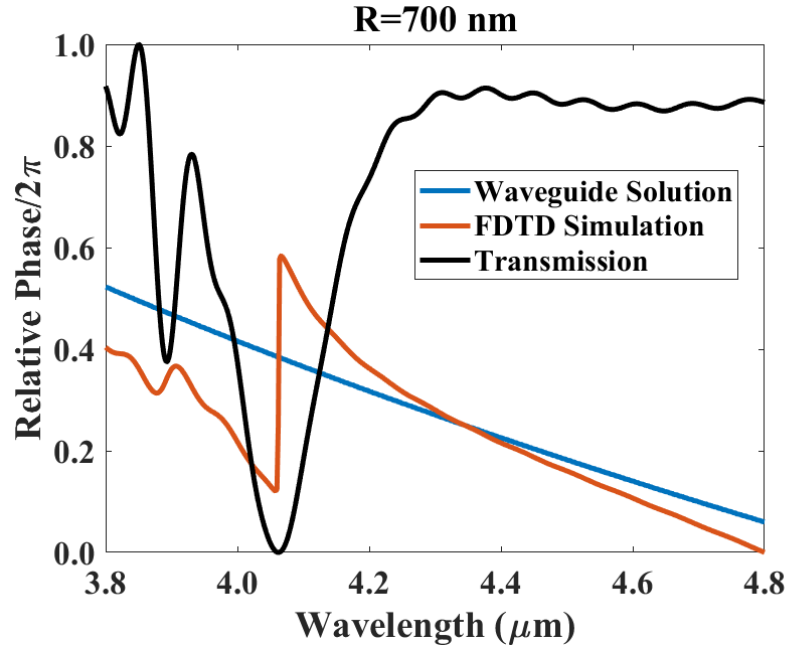


Figure 3.6 Transmission and phase response of a step-index cylindrical waveguide with a radius of $R=700$ nm operating in the on-resonance regime. Reprinted (or Adopted) with permission from [53]. Copyright 2019 American Institute of Physics.

Figure 3.5 shows the agreement with the numerical solution of the resulting waveguide equation and FDTD simulations. As seen in the figure, the calculated and simulated phase responses follow the same trend and the transmission response is almost constant in the off-resonance regime. However, in the on-resonance regime, there are strong jumps, which correspond to the scattering resonances, in both the simulated transmission and phase responses of these waveguides, as seen in Figure 3.6. These resonances abruptly disturb the optical response of waveguides, and as a result, prevent broadband operation.

In summary, step-index cylindrical waveguides enable polarization-insensitive broadband operation when they are operated in the off-resonance regime. Their polarization-insensitivity is a direct result of their circular symmetry, and their broad-band operation is provided by their waveguiding capability away from the resonance. Here, operating in the off-resonance regime is a critical requirement for such broadband operation since the resonances otherwise dominate over waveguiding and abruptly disturb the optical response of these waveguides.

3.3 Modelling and Simulation

3.3.1 Metasurface Unit Cells

To realize the proposed approach, we designed cylindrical nanopillars working as finite length step-index cylindrical waveguides, on top of a glass (SiO_2) substrate, as seen in Figure 3.7. The core of our waveguides is silicon (Si) and the cladding is air. Each phase element, nanopillar, constitutes a square unit cell with a side length of $1.8 \mu\text{m}$, where the height (H) of all nanopillars is $2 \mu\text{m}$ and their radii vary from 340 to 680 nm.

There are two important properties that lead us to choose silicon as the core material of our waveguides, apart from silicon's general and well-known advantages. One of them is its high index of refraction in our spectral band of interest. As seen from Equation (3.8), we have two variables to manipulate the phase response of a waveguide. The first one is height H and the second one is n_{eff} . The height allows us to linearly control the phase difference between pillars and the phase range that we can cover. However, increasing H increases the aspect ratio and, as a result, decreases feasibility of fabricating such a high aspect ratio nanostructure. Therefore, the variations of n_{eff} are kept large enough to make H reasonable.

On the other hand, this effective index is a function of the radius of the waveguide, the operation wavelength, and the refractive indices of both the core and the cladding. Its range is between the refractive index of the surrounding medium and the refractive index of the core material. As a result, a higher index contrast between the core and the cladding results in a larger possible difference in the phase response of different nanopillars. The other reason behind our material choice is the spectral position of the resonances. Using Si, we can obtain off-resonance operation for a wide enough range of pillar radius and height, which allows us to acquire the desired phase responses across our design spectral band.

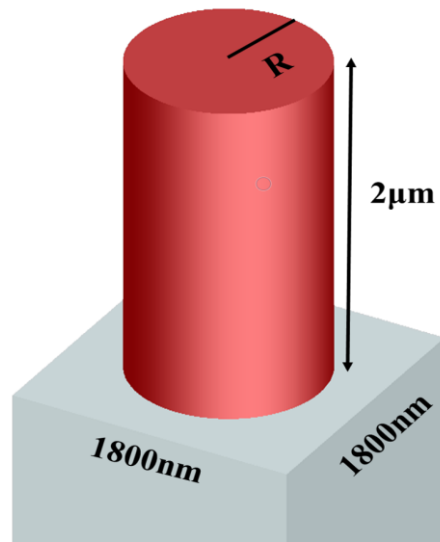


Figure 3.7 Side view of a unit cell: a Si nanopillar on top of a glass substrate. The substrate thickness taken to be infinite as it would be much thicker than the nanopillar height. Reprinted (or Adopted) with permission from [53]. Copyright 2019 American Institute of Physics.

Here, since the field confinement occurs inside high refractive index core, keeping the distance between pillars large enough ensures uncoupled operation for all pillars, as seen in Figure 3.7. As a result, the field at the cladding borders diminishes. This allows us to assume cladding radius to be infinite, as we did for the numerical calculations of our step-index cylindrical waveguides.

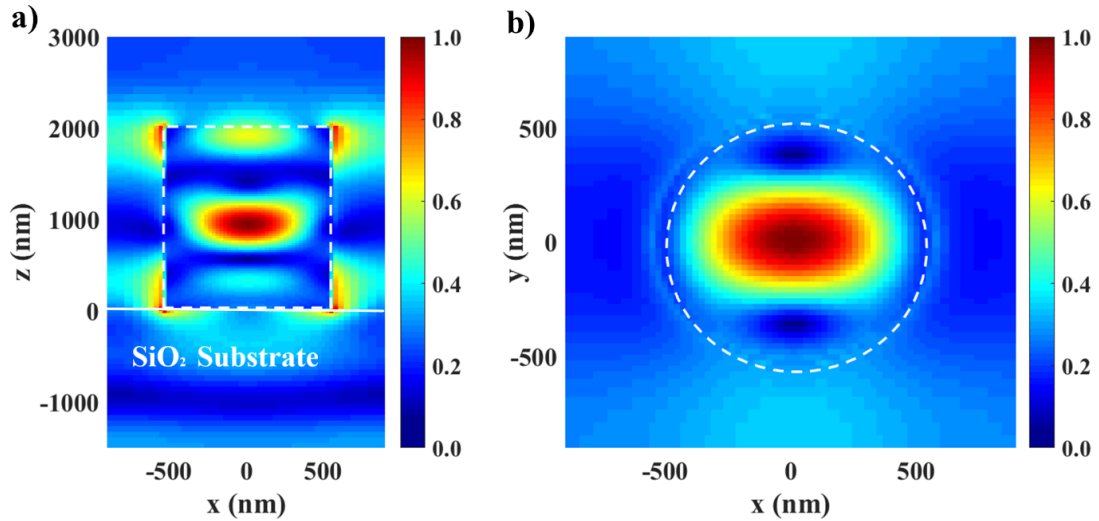


Figure 3.8 Electric field amplitude at a) xz cross section and b) xy cross section of the sample unit cell. The area enclosed by white dashed lines corresponds to the Si nanopillar. SiO_2 substrate is under the white line. Illumination is along $+z$ direction. The unit cell with nanopillar radius of 540 nm is chosen as the sample. The figure indicates that the field confined mostly inside the nanopillar and it fades at borders of the unit cell. Reprinted (or Adopted) with permission from [53]. Copyright 2019 American Institute of Physics.

To test the consistency of our model with the waveguide calculations, we compared the phase response obtained from our FDTD simulations and the numerical solution of waveguide approximation for our unit cell library, as shown in the Figure 3.9. As seen in the figure, since the waveguiding dominates over other optical effects on the phase response of these cylindrical nanopillars, the results obtained from both the waveguide solution and the FDTD simulations show great consistency proving the validity of our waveguiding concept.

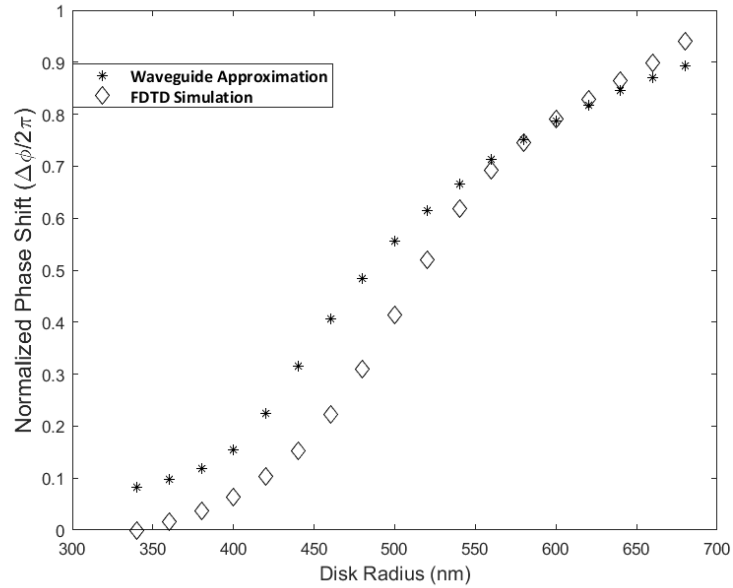


Figure 3.9 Comparison of the phase responses obtained from the FDTD simulations and the cylindrical waveguide solutions for our unit cell library. The wavelength of operation is $4.2 \mu\text{m}$.

As our model has proven its consistency, we simulated our unit cells' optical response over a broad spectral band from 3.8 to $4.8 \mu\text{m}$. Periodic boundary conditions are used at all x and y boundaries, and perfectly matched layer (PML) boundary conditions are used at z boundaries. The lower PML boundary along the z direction was put inside the glass substrate to obtain infinite effective thickness for the substrate. A plane wave source was located inside the glass substrate with forward injection ($+z$). A near-field monitor was located approximately $1 \mu\text{m}$ above the nanopillar. The transmission values were obtained directly from the near-field monitor, whereas the phase response obtained applying the far-field approximation to the fields obtained from the near-field monitor. To apply the far-field approximation, we used built-in "*farfieldexact*" function of the simulation program (Lumerical). The far-field response was calculated at $50 \mu\text{m}$ away from the nanopillars. The simulation results are shown in Figures 3.10 and 3.11.

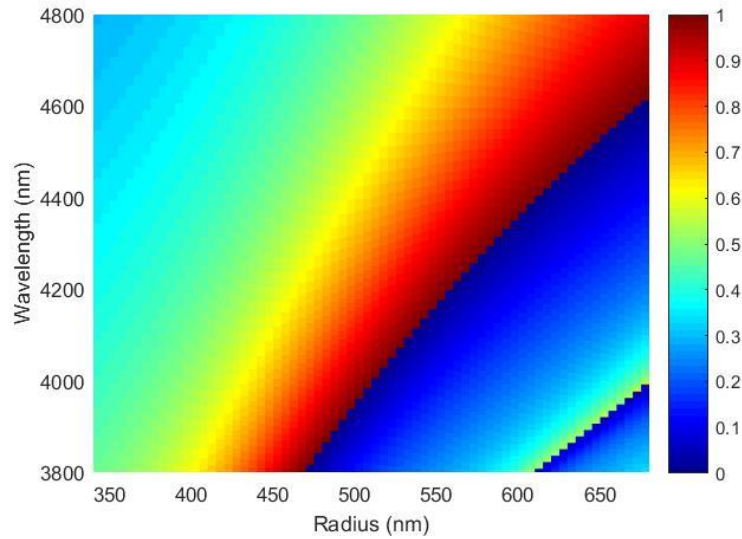


Figure 3.10 Phase response of the nanopillar unit cells as a function of the operating wavelength and the radius. Reprinted (or Adopted) with permission from [53]. Copyright 2019 American Institute of Physics.

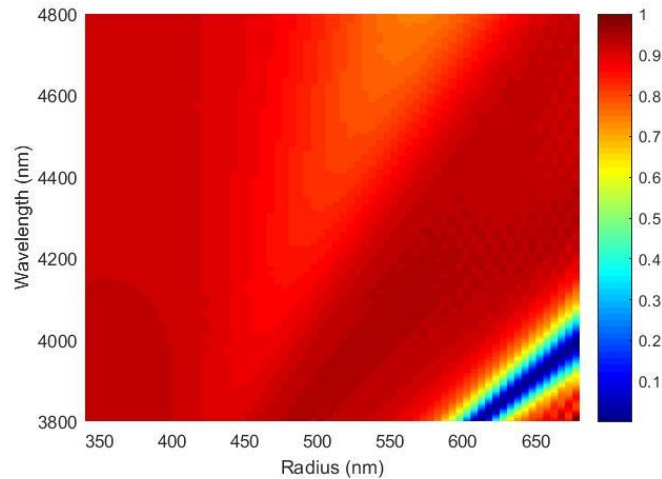


Figure 3.11 Transmission of the nanopillar unit cells as a function of the operating wavelength and the radius. The very low transmission values at shorter wavelengths for large radius values shows the resonant areas. Reprinted (or Adopted) with permission from [53]. Copyright 2019 American Institute of Physics.

We defined our spectral band of operation as the off-resonance spectral window of our unit cell library. As it can be seen from the transmission response of our unit cells (Figure

3.11), strong resonances emerge below 4.0 μm and relatively weak resonances emerge above 4.6 μm . As a result, we defined our spectral band of operation from 4.0 to 4.6 μm .

3.3.2 Metalens

The ability to spatially manipulate the phase of light enables us to shape the wavefront of light. By wavefront engineering, many optical components such as beam deflectors and converging and diverging lenses can be designed. Here, to indicate validity of our approach as a complete design, we designed a metalens as a proof-of-concept demonstration after defining our unit cell library and the spectral band of operation. Our lens was designed to have a focal length of 48 μm , which is a reasonable value for applications including focal plane arrays (FPAs) and various type infrared sensors. The focal length of lens is actually in the far field with respect to the far field criteria [56]: $k(r - a) \gg 1$, $r \gg a$ and $r \gg \frac{ka^2}{2}$ where r is the distance from an object of interest (assumed to be centered at the origin) to the observation point, k is the wave number and a is radius of the smallest sphere circumscribing the object. For a lens of interest, r is equal to focal length.

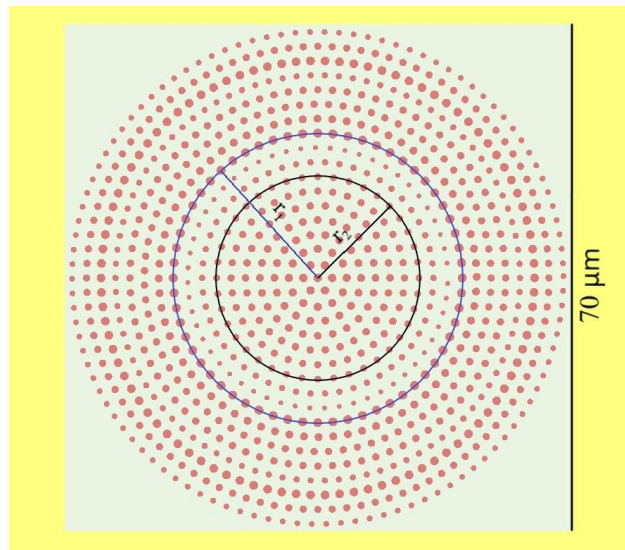


Figure 3.12 Top view of the lens with a 35 μm radius. Reprinted (or Adopted) with permission from [53]. Copyright 2019 American Institute of Physics.

The top view of the lens is shown in Figure 3.12. The nanopillars were placed on nested circles, where the radius values of the consecutive circles differ by $1.8 \mu\text{m}$ and the arc distance between the consecutive pillars on the same circle is also $1.8 \mu\text{m}$. The pillars were located to satisfy the required position dependent phase response of a flat lens that is given by Equation (3.9). The distance from the center, r , is the radius of the circles in this case. As a result, all pillars forming the same circle are identical. The design wavelength was chosen to be $4.2 \mu\text{m}$.

A simulation setup that is similar to the setup of unit cell simulations was used for simulating the metalens. Transmission was obtained directly from a near-field monitor. Electric and magnetic field intensities at the focal plane were calculated from the fields obtained from near-field monitor using “*farfieldexact*” function, as done for the unit cell simulations.

3.4 Results and Discussion

Focusing is confirmed from the field intensity distribution at $y=0$ (xz) plane, Figure 3.13. To obtain the focal length, the field intensity is calculated along optical axis to determine the focal length. As shown in Figure 3.14, the focal length is $48 \mu\text{m}$ at design wavelength, $50 \mu\text{m}$ at the lower border and $46 \mu\text{m}$ at the higher border of the spectral band of operation.

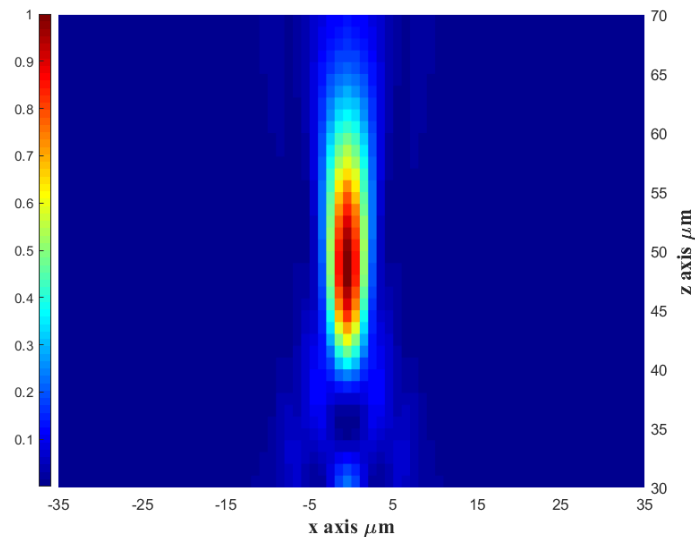


Figure 3.13 Field intensity at $y=0$ (xz) plane

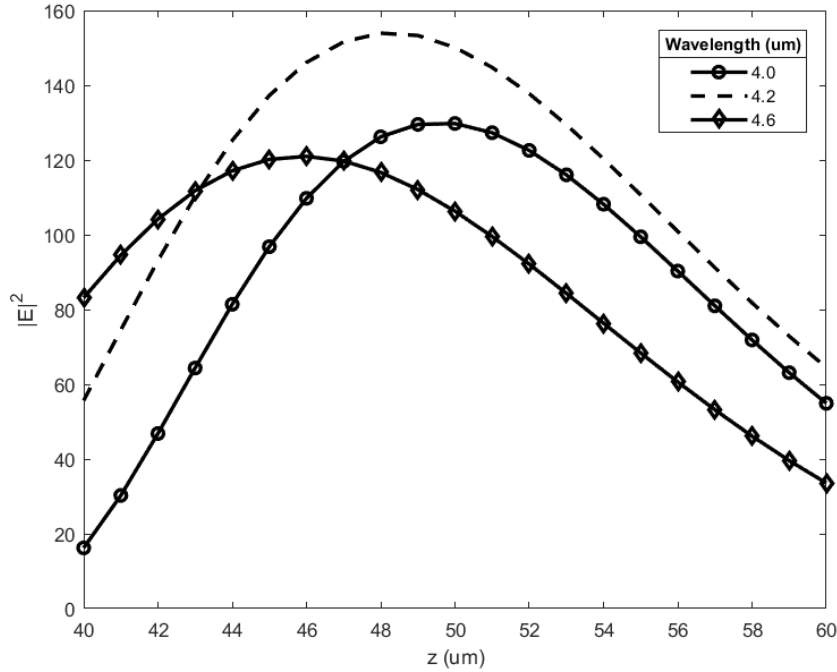


Figure 3.14 Field intensity along the optical axis at the design wavelength (4.2 μm) and the borders of the spectral band of operation (4.2 μm and 4.6 μm).

The focusing behavior at our design wavelength (4.2 μm) can also be seen from various perspectives in Figures 3.15, 3.16 and 3.17. Figures 3.15 and 3.16 show the focal planes of the lens under TM and TE illuminations, respectively, and Figure 3.17 depicts the horizontal cuts of these planes. As seen from both the focal planes and their horizontal cuts, the focal spot is identical in the main lobe for the two perpendicular polarizations indicating the polarization insensitivity. The FWHM value is found to be 0.40λ , where the diffraction limit is calculated as 0.36λ . The focal spot radius is determined as 4.0 μm , which is approximately twice of the FWHM. The obtained focusing efficiency, which is calculated as the ratio of the total light intensity at the focal spot to the total transmitted light, is 94.0%. The absolute efficiency, which is defined as the ratio of the total light intensity at the focal spot to the incident light intensity, is found as 67.7%.

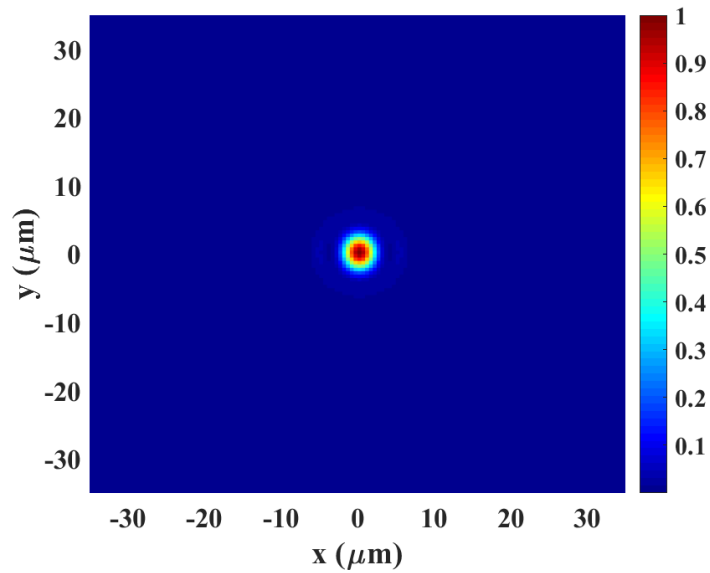


Figure 3.15 Light distribution at the focal plane ($z=48 \mu\text{m}$ plane) of metalens under $4.2 \mu\text{m}$ TM polarized light. Intensities are normalized. Reprinted (or Adopted) with permission from [53]. Copyright 2019 American Institute of Physics.

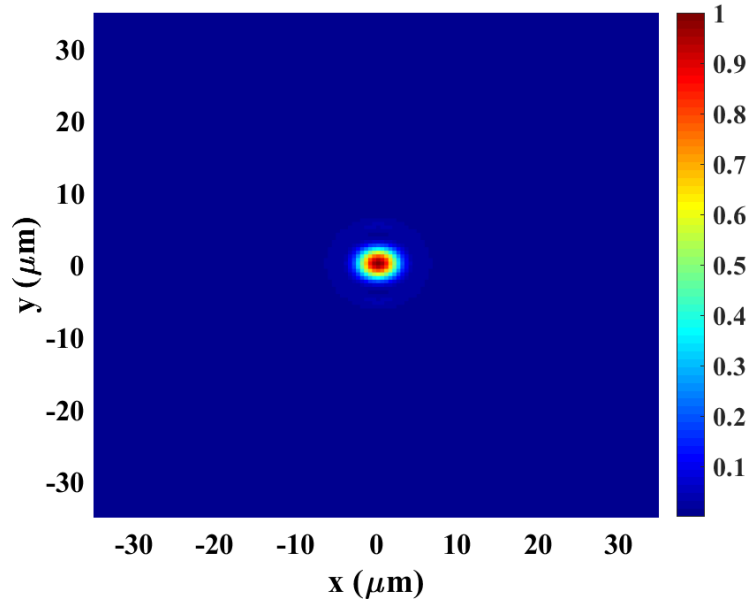


Figure 3.16 Light distribution at the focal plane ($z=48 \mu\text{m}$ plane) of metalens under $4.2 \mu\text{m}$ TE polarized light. Intensities are normalized. Reprinted (or Adopted) with permission from [53]. Copyright 2019 American Institute of Physics.

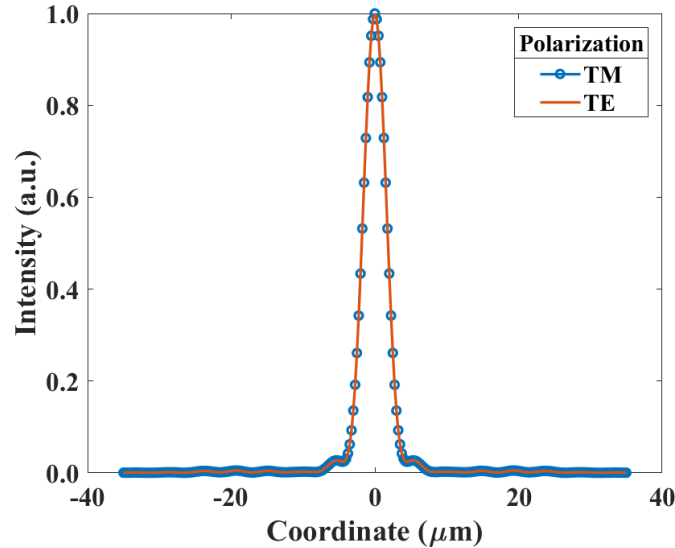


Figure 3.17 Intensity profile in the focal plane under TE and TM illumination. Intensities are normalized. Reprinted (or Adopted) with permission from [53]. Copyright 2019 American Institute of Physics.

There are two main parameters to determine the broad-band performance of a focusing lens: the change of the focal length and the change in the focusing efficiency. The designed lens maintains focusing behavior with $<5\%$ decrease of efficiency and $<5\%$ shift of focal distance within the defined spectral band of operation. Figure 3.18 shows the horizontal cuts of the focal plane at various wavelengths in the operating band indicating permanency of the focusing behavior. As seen in Figure 3.19, the focal length stays constant for an almost 600 nm of wavelength span around the design wavelength and the maximum focal shifts are $\pm 2 \mu\text{m}$. The efficiency values were calculated at the focal distance of the design wavelength. As seen from Figure 3.20, the relative efficiency is always higher than 90% and the absolute efficiency is almost 70%. Both efficiencies only slightly change across the entire operating band.

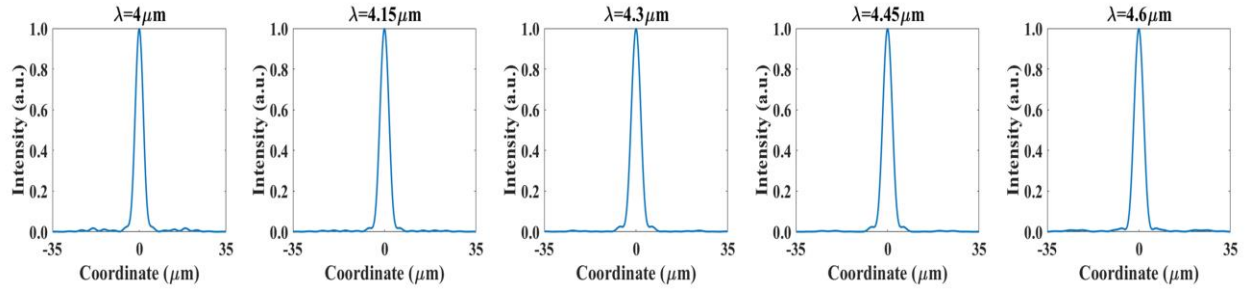


Figure 3.18 Intensity profile in the focal plane under illumination at 4.00, 4.15, 4.30, 4.45 and 4.60 μm . Reprinted (or Adopted) with permission from [53]. Copyright 2019 American Institute of Physics.

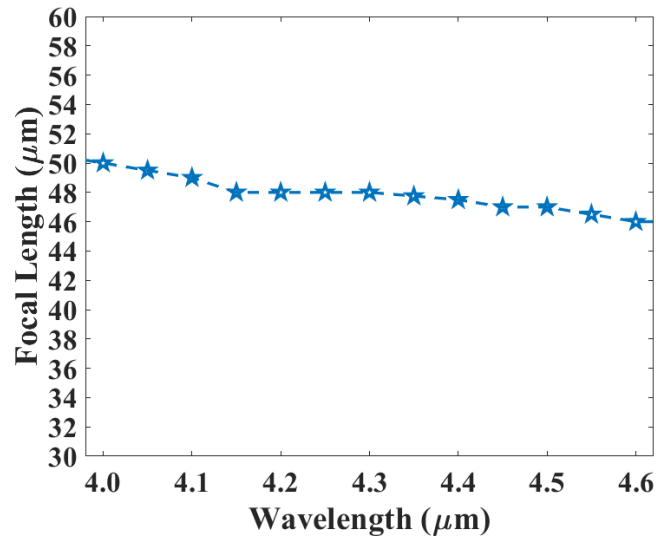


Figure 3.19 Focal distances of the metalens in the spectral band of operation. Reprinted (or Adopted) with permission from [53]. Copyright 2019 American Institute of Physics.

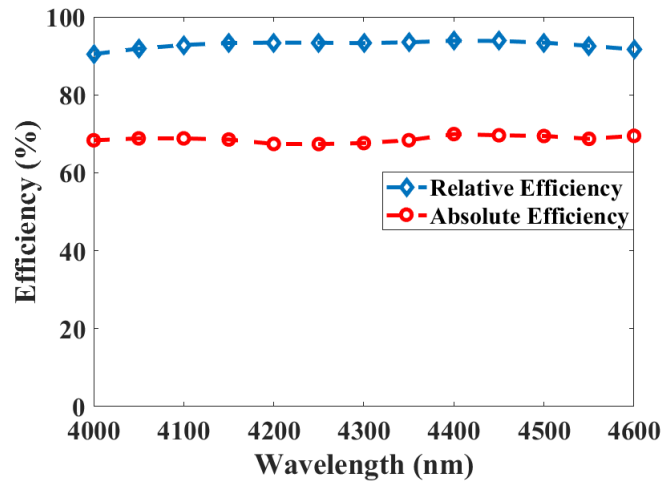


Figure 3.20 Relative and absolute efficiencies of the metalens in the spectral band of operation. The efficiency values were calculated at 48 μm , which is the focal length at the design wavelength. Reprinted (or Adopted) with permission from [53]. Copyright 2019 American Institute of Physics.

Table 3.1 Performance metrics of previously reported metalenses and comparison to this work. Reprinted (or Adopted) with permission from [53]. Copyright 2019 American Institute of Physics.

	$\frac{\text{FWHM spot size}(\lambda)}{\text{Diffraction limit}(\lambda)}$	Focusing efficiency	Polarization	Wavelength (nm)	Aspect ratio	Numerical aperture
[10] [*]	0.51/0.5	~52%	Insensitive	1550	4.7	0.97
[11] ^{**}	~0.7/0.625	86%	Circular	405	3.86	0.8
[12] ^{**}	~0.255/2.5	20%	Circular	500	~2.8	0.2
[13] ^{**}	~0.64/0.6	60%	Insensitive	660	~2.7	0.85
[14] [*]	1.56/1.33	80%	Insensitive	3200	~2.2	0.2
[15] [*]	1.94/1.72	~72%	Insensitive	1550	7	0.29
[16] ^{**}	18.7/6.25	10%	N/A	1550	5.3	0.04
[17] ^{**}	5.35/4.64	~42%	Circular	560	17.8	0.106
This Work [*]	~0.4/0.36	68%	Insensitive	4200	~3	0.73

^{*}simulation result; ^{**}measurement result.

In Table 3.1, we compared performance of the proposed structure with the previous reports, in terms of the typical performance metrics. Some of the values given in the table belong to broad-band or multi-wavelength designs while the rest belong to single-

wavelength designs. We chose the wavelength with the highest efficiency value for the multi-wavelength designs, and the values obtained for the central wavelength for the broad-band designs. In measurement result, a slight decrease in the FWHM and a 5%-10% decrease in absolute efficiency may be expected due to possible fabrication imperfections compared to the simulation results. As the field is highly confined in the case of pillars and the distance between the adjacent pillars are far enough, it is not expected to observe a major decrease in the performance resulting from mutual coupling.

Table 3.2 Figure of merits (FoMs) defined to quantitatively analyze broad-band performance. Here F is the focal length, λ is the operating wavelength and η is the percentage efficiency. Reprinted (or Adopted) with permission from [53]. Copyright 2019 American Institute of Physics.

FoM 1 ($\%nm^{-1}$)	$[\Delta F / (F * \Delta \lambda)] * 100$
FoM 2 ($\%nm^{-1}$)	$\Delta \eta / \Delta \lambda$
FoM 3 ($\%nm^{-1}$)	$[(\Delta \eta / \eta) / \Delta \lambda] * 100$

Broadband performance of a focusing lens can be evaluated from two major points of view. These are the shift of the focal distance and change in the focusing efficiency over the operating wavelength. To quantitatively compare our proposed structure with the achromatic designs and similar geometries reported in literature, we defined three figure of merits (FoMs) in Table 3.2, each of which underlines different aspects of the broadband focusing behavior. To analytically evaluate the achromaticity from the focal shift perspective, FoM1 is defined as the percentage shift of the focal distance per change in the operating wavelength, which is ideally equal to zero for perfect achromatic lenses. To evaluate the efficiency aspect of achromaticity, we defined FoM2 and FoM3. The former only considers the change in efficiency with respect to the change in operating wavelength. The latter also takes into account the efficiency at the design wavelength, which is an important performance metric but is not directly related with the achromaticity. As it can be directly understood from the definitions of these FoMs, lower values indicate better performance. The calculated FoMs for different designs are summarized in Table 3.3. Here, only the best previous reports in terms of these defined

FoM are included. As seen in the table, our design outperforms all of these previous reports in terms of both the focal distance shift and the efficiency change.

Table 3.3 Comparison of previous reports and this work in terms of the defined FoMs. Reprinted (or Adopted) with permission from [53]. Copyright 2019 American Institute of Physics.

	FoM 1 (% nm^{-1})	FoM 2 (% nm^{-1})	FoM 3 (% nm^{-1})
[10]**	~0.11	0.1	2.4×10^{-3}
[11]**	~0.16	Not reported	Not reported
[12]**	~0.016	0.1	0.01
[17]**	~0.04	~0.16	2.9×10^{-3}
This Work*	~0.010	4.75×10^{-3}	5.9×10^{-5}

*simulation result; ** measurement result.

3.5 Summary

To sum up, we proposed and demonstrated a new method of the wavefront control based on off-resonance waveguiding to achieve polarization insensitivity and broadband operation. As a proof of concept, we showed a polarization insensitive dielectric microlens operating between 4.0 and 4.6 μm with >94% relative and >67% absolute efficiencies. The proposed methodology can be applied to every desired wavelength range via a proper choice of the core material. These findings indicate that achieving polarization insensitive broad-band operation with high efficiency in the mid-wave range is a critical step towards implementing metasurface concept for practical applications in integrated optics in the infrared.

Chapter 4

Infrared and Visible Polarization-insensitive Achromatic All-dielectric Metasurfaces

4.1 Availability of High-Index Material and Narrow Off-Resonance Window Problem

Significance of achieving polarization-insensitive wavefront control over wide spectral bands is explained in Chapter 3. In the same chapter, off-resonance waveguiding approach has been proposed as an effective solution to address this need, and demonstrated in mid-wave infrared band. Superior performance of this approach has been confirmed with full electromagnetic solutions. However, waveguiding approach has strict requirements. First of all, the material used as the core of the waveguide must be lossless and has a high refractive index. And more critically, this approach requires a large off-resonance window to provide broad-band operation. Neither fully lossless materials with high enough refractive indices nor wide enough off-resonance windows are available at every portion of electromagnetic spectrum. In the visible region, for example, high refractive index materials, such as silicon, introduce large absorption losses at shorter wavelengths. And,

off-resonance windows of nanopillars made from lossless dielectrics, such as TiO_2 and SiN_x , cannot cover the visible region. As a result, although the governing physical phenomena are universal, this approach cannot be applied successfully to certain portions of the electromagnetic spectrum due to strict material requirements and scarcity of proper materials.

Here, to address this problem, we propose the coupled metasurfaces approach. This approach also depends on the index contrast between unit structures and surrounding media. However, this dependency is much looser in this approach than it is in the off-resonance waveguiding. Additionally, the dimensions and locations of unit structures significantly broaden the off-resonance window. As a result, this approach is immune to resonances by its nature.

We conduct a systematic study of the phase responses of coupled cylindrical scatterers under linear, square and hexagonal packing schemes. For this part of the work, a hypothetical material is used as a starting point. Then, to show generality of the approach, geometrical parameters are scaled down to the infrared and visible regions with proper material choices. And finally, two lenses are designed as proof-of-concept demonstrations, where one of them is operated in the infrared and the other, in the visible region. A significant increase in the operation bandwidth is confirmed via full electromagnetic simulations.

4.2 Coupled Metasurfaces Approach

Current metasurface approaches use unit cells to spatially manipulate the wavefront [1, 9-31]. In general, those unit cells are designed as nanostructures placed into square, rectangular or hexagonal lattices. Their optical response is modified by modifying dimensions of these nanostructures. To ensure that the optical responses of those unit cells are independent from their neighbors, the lattice constants are kept high [53].

In our coupled metasurface approach, there is no defined unit cell. Additionally, all nanostructures constituting the metasurface are exactly the same, in contrary to the literature. The optical response of these nanostructures depends on the distance between them and neighboring nanostructures.

Coupled metasurfaces approach is based on manipulating light by tuning the strength of coupling between dielectric nanostructures. To take advantage of their circular symmetry, we designed our nanostructures as cylindrical nanopillars, which have the same geometry (Figure 3.7) with the ones used in the off-resonance waveguiding approach but smaller in diameter.

These nanostructures act as efficient optical scatterers. When the scatterers are placed close enough to each other, they become coupled. The field scattered from these coupled scatterers confine between the walls of these scatterers. This confined field determines the effective index and, as a result, the phase response of the medium. The confined field intensity depends on the coupling strength. And, the strength of this coupling depends on the scattering efficiency of scatterers and wall-to-wall distance (gap) between them. This chain of dependencies allows us to control phase response of the medium by controlling the gap between the scatterers. As the gap decreases, the coupling strength and thus the E-field confined between the scatterers increase. This, in turn, increases the effective refractive index, and so the phase response of effective medium, and vice versa.

4.2.1 Coupled Scatterers

Coupling between dielectric nanostructures has been studied in isolated dimers [57] and also oligomer [58] configurations have been investigated. However, their behavior in the coupled arrays has not been studied to the best of our knowledge. Here, we studied the phase response of coupled dielectric nanopillars in linear, square and hexagonal packing configurations using full electromagnetic simulations. For this systematic study, we start with a hypothetical material with a refractive index of 4, and we make all simulations using a monochromatic plane wave source at the field injection wavelength of 4 μm . The wall-to-wall distance between scatterers is changed from 20 to 800 nm.

4.2.1.1 Linear Packing Scheme

The periodicity along y direction is kept $2\ \mu\text{m}$ to ensure uncoupled operation along y axis, and x axis is chosen as the coupling axis. The periodicity along x direction is tuned as $T=2r+g$, where T is periodicity, r is radius of nanopillars (the scatterers) and g is wall-to-wall distance (gap) between the scatterers.

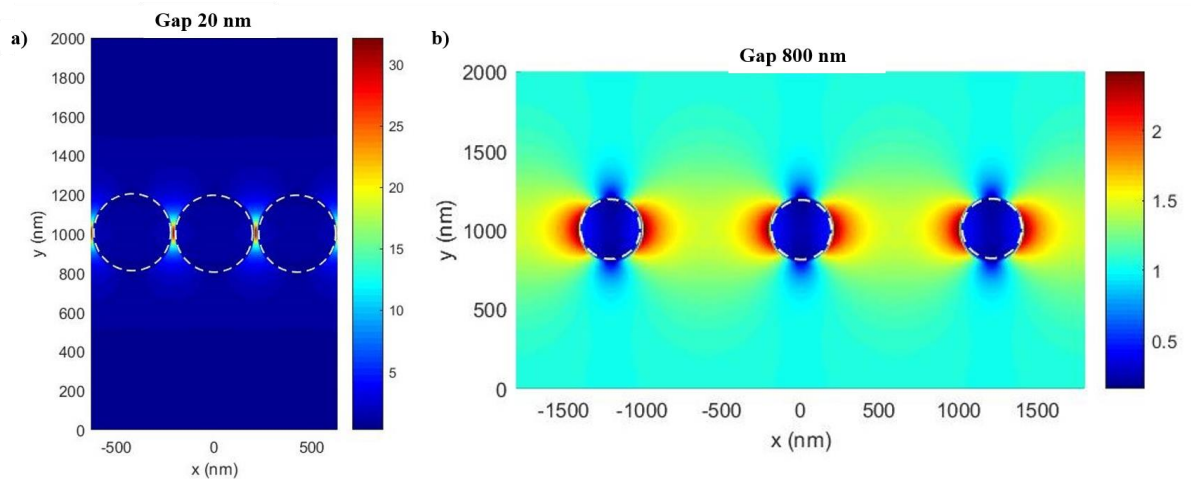


Figure 4.1 Electric field distribution over $z=1\ \mu\text{m}$ plane of linearly packed scatterers under x -polarized illumination. a) The gap is 20 nm. b) The gap is 800 nm. The white dashed circles correspond to nanopillars.

Scatterers that are placed far enough to each other (Figure 4.1b)) are uncoupled scatterers. Their optical responses are independent from each other. However, when the distance between scatterers decreases, electromagnetic coupling arises between them. The strength of this coupling increases as the distance (gap) between them decreases. Strong coupling of scatterers results in strong field confinement and increases peak intensity as seen from Figure 4.1a). This strong field confinement corresponds to increased effective index and thus increased phase shift introduced by medium as seen from Figure 4.2.

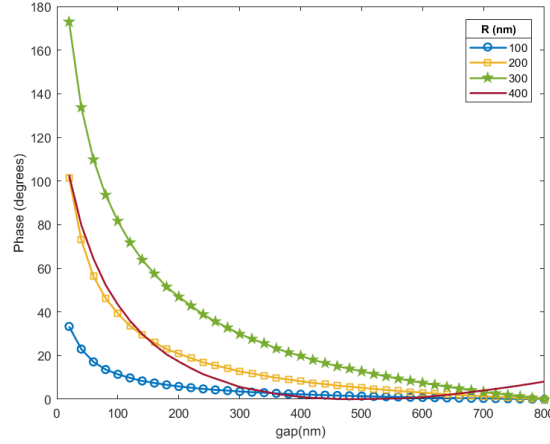


Figure 4.2 Phase response of medium (linearly packed scatterers under x -polarized illumination) versus the gap between scatterers parametrized with respect to scatterer radius.

Since all the scatterers, nanopillars in this case, are identical, the relative phase shift introduced by individual nanopillars is zero, independent from their radius. However, the collective optical response, and the relative phase coverage, of these coupled nanopillars is strongly dependent on the radius, as seen from Figure 4.2. The effect of radius on the relative phase coverage is the combination of radius effect on the scattering efficiency, which is one of the critical factors determining the coupling strength, and that on the filling factor (FF), which is the ratio of high index material over entire volume (area).

Mathematically,

$$\Delta\varphi = \Delta\varphi_C + \Delta\varphi_{FF} \quad (4.1)$$

where $\Delta\varphi$ is total phase coverage, $\Delta\varphi_C$ is phase coverage caused from coupling, and $\Delta\varphi_{FF}$ is the phase coverage introduced by FF. Differentiating with respect to the radius,

$$\frac{d\Delta\varphi}{dr} = \frac{d\Delta\varphi_C}{dr} + \frac{d\Delta\varphi_{FF}}{dr} \quad (4.2)$$

The effect of radius on FF-originated phase coverage, $\frac{d\Delta\varphi_{FF}}{dr}$, is always positive. However, the effect of radius on the coupling-originated phase coverage, $\frac{d\Delta\varphi_C}{dr}$, becomes negative after some optimum point. After the optimum point, the scattering efficiency decreases

since the incident fields start to couple into the guided modes of nanopillars (Chapter 3.2.1) rather than being scattered by them. Note that, $\frac{d\Delta\varphi}{dr}$ is still positive up to the point where $\frac{d\Delta\varphi_C}{dr} = -\frac{d\Delta\varphi_{FF}}{dr}$. This is the optimum point, the optimal radius, for the maximum relative phase coverage. The relative phase coverage decreases by further increasing the radius beyond this point (Figure 4.2).

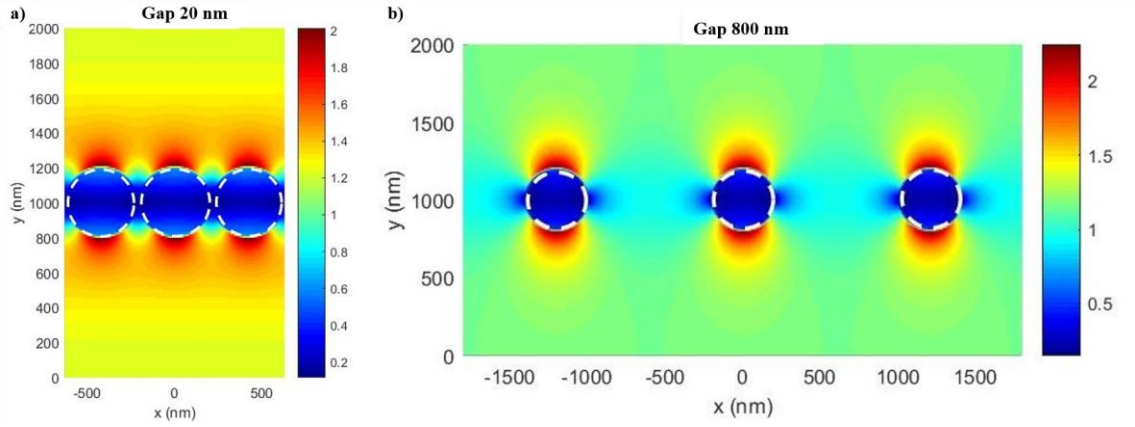


Figure 4.3 Electric field distribution over $z=1 \mu\text{m}$ plane of linearly packed scatterers under y -polarized illumination. a) The gap is 20 nm. b) The gap is 800 nm. The white dashed circles correspond to the nanopillars.

In the case of y -polarized incidence, decreasing the gap between the scatterers does not create strong electromagnetic coupling between these scatterers even at extremely high proximity (Figure 4.3a) since the polarization axis of incident, and thus the scattered, light is perpendicular to the coupling axis. As seen from Figure 4.3, although there is weak coupling between the scatterers when the gap is too small, the peak intensity does not increase with proximity.

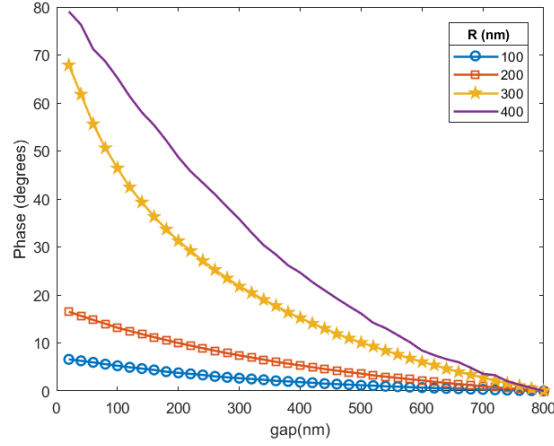


Figure 4.4 Phase response of medium (linearly packed scatterers under y -polarized illumination) versus the gap between scatterers parametrized with respect to scatterer radius.

Since the coupling is weak and limited to too small gap values, the effect of coupling could be ignored in the case of y -polarized incidence. Eqn. 4.2 becomes

$$\frac{d\Delta\varphi}{dr} = \frac{d\Delta\varphi_{FF}}{dr} > 0 \quad (4.3)$$

as $\frac{d\Delta\varphi_C}{dr} = 0$, and $\frac{d\Delta\varphi_{FF}}{dr} > 0$. As seen from Figure 4.4, the relative phase coverage is smaller than it is under x -polarized incidence but it keeps increasing with the radius on the contrary to the case of x -polarized incidence (Figure 4.2).

4.2.1.2 Square Packing Scheme

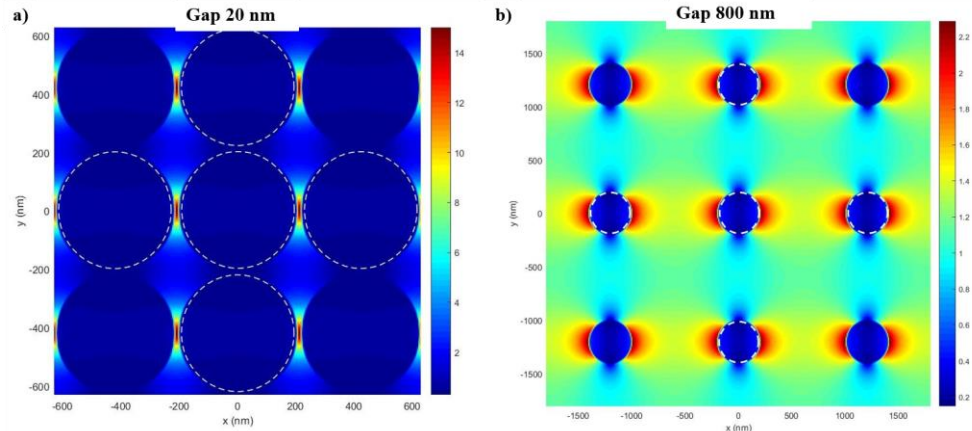


Figure 4.5 Electric field distribution over $z=1 \mu\text{m}$ plane of square packed scatterers under x -polarized illumination. a) The gap is 20 nm. b) The gap is 800 nm. The white dashed circles correspond to the nanopillars.

Filling factor and average confined field are higher for the square packed pillars than they are for the linear packed ones since the square packing is a denser scheme than the linear packing. Additionally, the square packing provides polarization-insensitive operation as this packing has the same symmetry along both x and y axes.

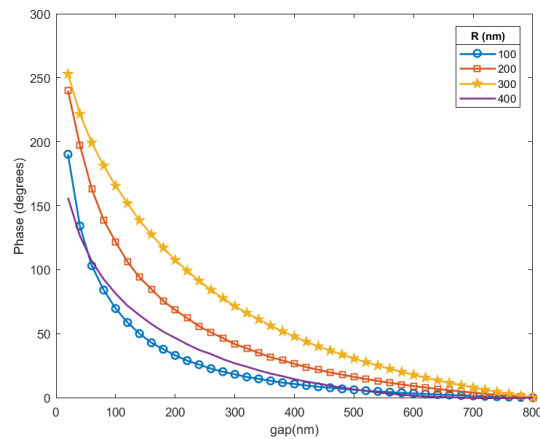


Figure 4.6 Phase response of medium (square packed scatterers) versus the gap between scatterers parametrized with respect to scatterer radius.

$\Delta\varphi$ is increased in the square packing configuration (Figure 4.6) compared to the linear packing (Figure 4.2 and 4.4). This increase is a collective result of both increased coupling ($\Delta\varphi_c$) and increased FF ($\Delta\varphi_c$). As seen from Figure 4.6, the relative phase coverage of nanopillars with a radius of 400 nm is the smallest. Comparing this result with those shown in the Figure 4.2 indicates that the effect of coupling on the phase response is more dominant in the square packing scheme than it is in the linear packing.

4.2.1.3 Hexagonal Packing Scheme

Based on the findings from the linear packing and square packing simulations, we design our coupled metasurface phase elements. We chose the hexagonal packing scheme for our scatterers. Due to its high density, coupling strongly dominates on the phase response of scatterers. This provides polarization-insensitive operation due to its symmetry. Strong coupling under both x and y polarized illumination is shown in Figure 4.7.

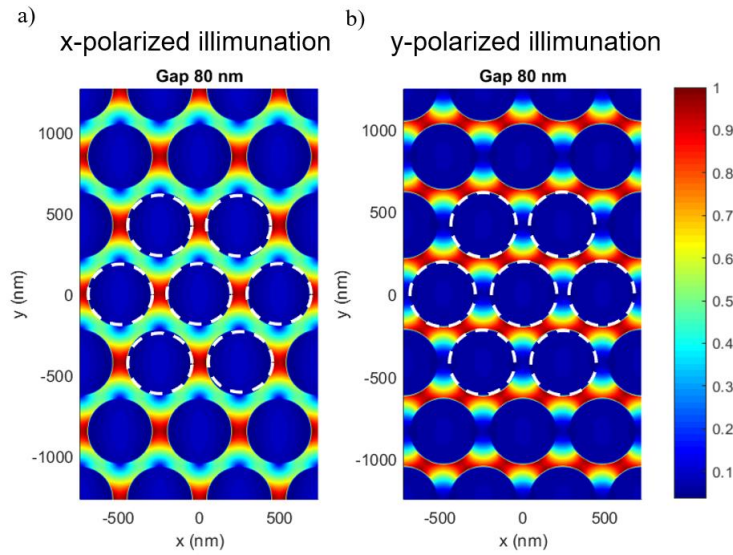


Figure 4.7 Normalized electric field distribution over $z=1 \mu\text{m}$ plane of hexagonally packed scatterers under a) x -polarized illumination and b) y -polarized illumination. The gap is 80 nm. The white dashed circles correspond to the nanopillars.

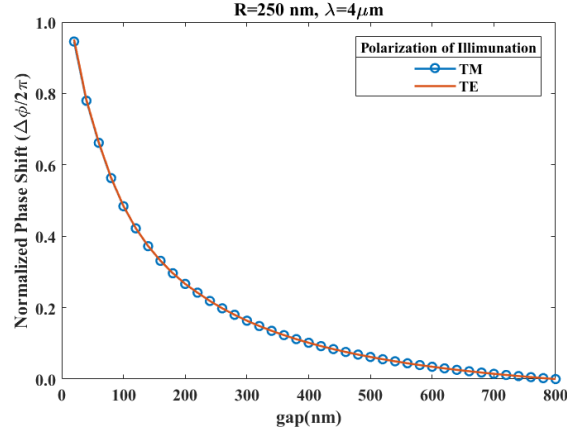


Figure 4.8 Phase response of medium (hexagonally packed scatterers) versus the gap between scatterers under x (TM) and y (TE) polarized illumination.

As explained for the linearly packed scatterers, there is an optimum radius providing maximum $\Delta\phi$. We find the optimum radius value to be 250 nm for our hypothetical material with a refractive index of 4 (at 4 μm wavelength). As seen in Figure 4.8, fully polarization-insensitive coverage of the phase change range of 0 to 2π in its entirety is achieved.

4.3 Generality of Approach

After defining our scatterer dimensions, we scaled these dimensions to the infrared and the visible wavelengths by using silicon (Si) for the infrared and titanium oxide (TiO_2) for the visible region. We chose these materials as they have high refractive indices and they are lossless at the corresponding spectral bands of operation.

Table 4.1 Scaling parameters of scatterers.

Material	λ (nm)	n	R (nm)	H (nm)	Gap range (nm)
Made up	4000	4.00	250	2000	20 to 800
Si	3200	3.43	233 ~ 235	1973~2000	20 to 800
TiO_2	550	2.43	56 ~ 55	577 ~ 580	5 to 200

The scaled dimensions together with the scaling parameters are shown in Table 4.1. The radius of pillars is scaled as $R' = Rn\lambda' / n'\lambda$ and their height is scaled as $H' = \frac{H(n-n_{med})\lambda'}{(n-n_{med})\lambda}$, where n is the refractive index of the material, n_{med} is the refractive index of surrounding medium and λ is the operation wavelength. Transmission and phase responses of the corresponding scatterers are shown in Figure 4.9.

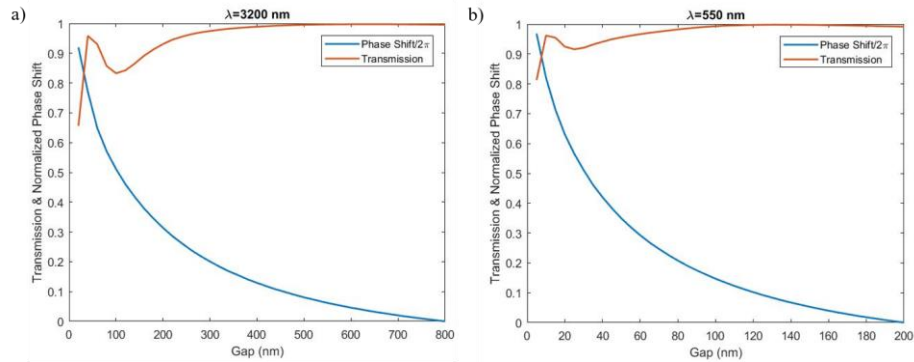


Figure 4.9 Transmission and phase responses of hexagonally packed a) silicon nanopillars at 3.2 μm wavelength and b) titanium oxide nanopillars at 550 nm wavelength.

Fabry-Pérot reflections arise with the increased packing density (decreased gap) in the transmission response of the silicon nanopillars (Figure 4.10a)). These reflections cause significant loss (up to 45%) as seen in Figure 4.10a). To avoid this loss, we optimized transmission response of our Si nanopillars by placing an Al_2O_3 phase matching layer with a thickness of 600 nm (Figure 4.11). The optimized transmission response is shown in Figure 4.10b).

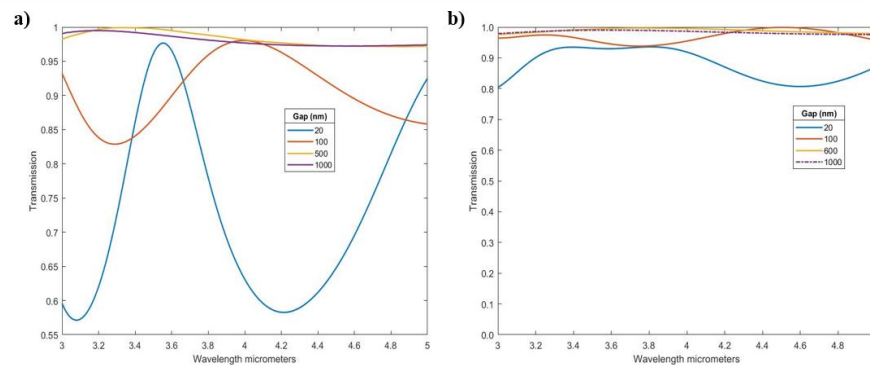


Figure 4.10 Transmission response of hexagonally packed a) silicon and b) silicon-aluminum oxide (optimized) pillars using various gap values.

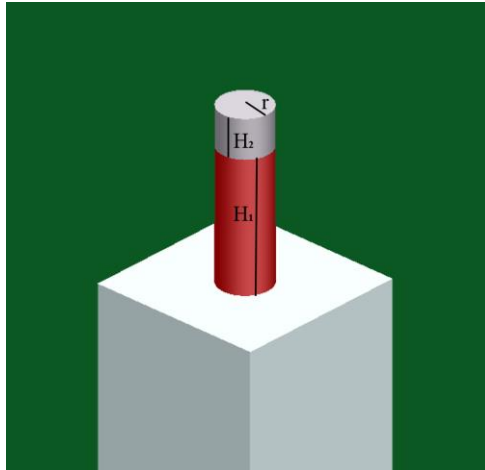


Figure 4.11 Schematic of transmission optimized nanopillars. The red cylinder is Si and the white cylinder on top of it is Al_2O_3 . H_1 is $2\ \mu\text{m}$, H_2 is $600\ \text{nm}$ and r is $235\ \text{nm}$. The white prism under the pillar represents SiO_2 substrate.

4.4 Results and Discussion

Using the unit scatterers obtained from the scaling, we design two metalenses, one of which is operating in the infrared and the other of which is operating in the visible region, as proof-of-concept demonstrations.

4.4.1 Metalens in the Infrared Region

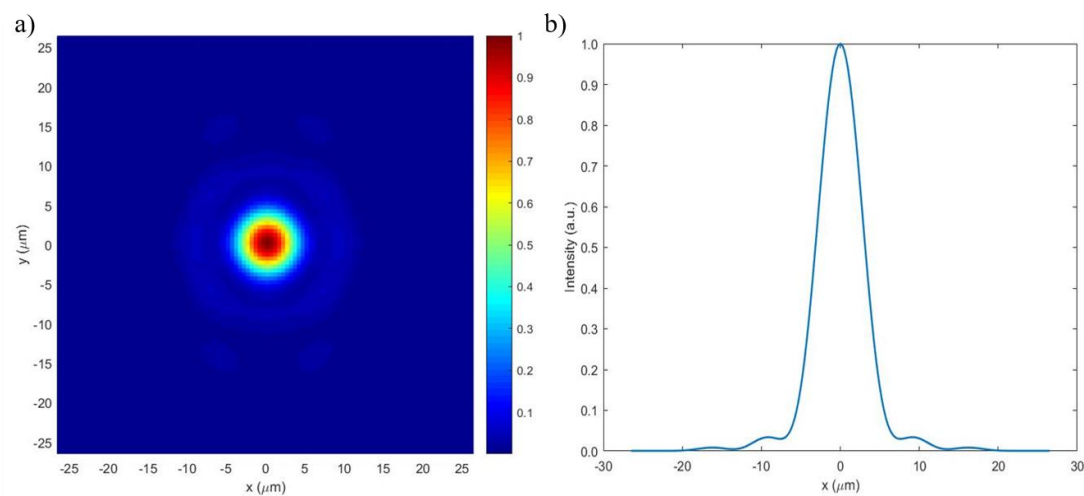


Figure 4.12 a) Focal plane and b) its horizontal cut for the metalens working in the infrared region. The operation wavelength is $3.2\ \mu\text{m}$. The lens diameter is $56\ \mu\text{m}$.

Table 4.2 Performance of Coupled Metalens

Wavelength (nm)	Relative Efficiency (%)	Absolute Efficiency (%)	Focal Distance (μm)
4200	92.3	89.0	95.75
3200	93.4	90.1	100.75
2200	88.5	79.7	110.75

The focusing behavior at our design wavelength (3.2 μm) can be seen from Figure 4. 12, which shows the focal planes of the lens and the horizontal cut of this plane. The full-width-half-maximum (FWHM) value is found to be 0.957λ , where the diffraction limit is calculated as 0.950λ . The focal spot radius is determined as 2.0 μm (approximately twice of the FWHM). The obtained focusing efficiency, absolute efficiency, and focal distance values at the operation wavelengths of 2.2, 3.2, and 4.2 μm are shown in Table 4.2. As seen in Table 4.2, the metalens maintains high efficiency focusing along a wide spectral band of operation with a maximum of 10% focal distance shift.

4.4.1 Metalens in the Visible Region

Figure 4.13 shows the performance of the coupled lens in the visible region. From 450 to 650 nm, the lens maintains perfectly achromatic operation. Since strong resonances cannot be avoided in the violet part of the visible spectrum, the maximum focal shift occurs in this part. The maximum focal distance shift is approximately 10%, which is still acceptable. Thanks to high transmission efficiency of the metalens, the difference between relative and absolute focusing efficiencies changes between 5% and 10%. The lens maintains high efficiency focusing across the entire visible spectrum.

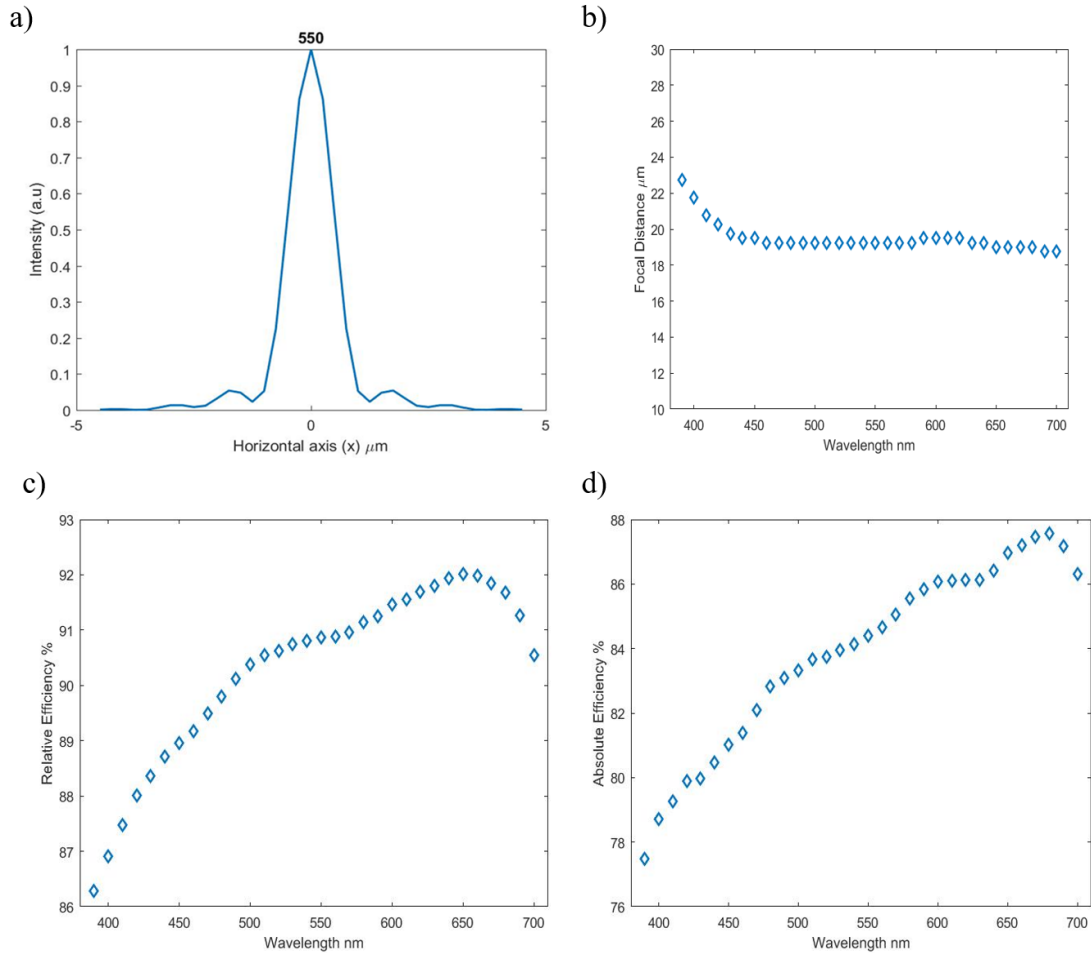


Figure 4.13 a) Intensity profile in the focal plane of lens. The full-width-half-maximum is $\sim 0.5 \mu\text{m}$. b) Focal length of the lens across the visible spectrum. c) Relative and d) absolute focusing efficiencies of the lens across the visible spectrum. The lens diameter of lens is $20 \mu\text{m}$.

In summary, we systematically studied the phase response of coupled scatterers for various packing configurations. Then, based on our study, we proposed and demonstrated a method enabling polarization-insensitive control of wavefront over wide spectral bands. We showed the generality of the proposed method for every desired wavelength range via a proper material choice. As a proof of concept, we showed two polarization-insensitive dielectric metalenses operating in the IR and visible region. The lenses have shown high performance along their spectral bands of operation.

Chapter 5

Conclusion

Metasurfaces allow for great possibilities on light manipulation. The metasurface concept enables us to manipulate light in sub-wavelength thicknesses and with sub-wavelength spatial resolution. Plasmonic metasurfaces that consist of metallic nanostructures were the precursor examples of such metasurfaces. Later, dielectric metasurfaces were introduced, which now attracts great interest because of their higher efficiencies than that of plasmonic metasurfaces. However, current approaches on the dielectric metasurfaces suffer from fundamental limitations either on the operation bandwidth or on the polarization dependency.

In this thesis work, we studied dielectric metasurface phase elements using full electromagnetic solutions and numerical calculations. We used the commercial program Lumerical FDTD solutions and MATLAB for numerical calculations. We aimed and achieved to solve the problems of both the narrow operation bandwidth and polarization sensitivity, and to increase the performance level of metasurfaces. To this end, we proposed and demonstrated two novel approaches providing universally polarization-insensitive achromatic operation. We designed and showed three metalenses operating in the infrared and visible regions as proof-of-concept demonstrations.

Using step-index cylindrical waveguides and avoiding effects of the scattering resonances in this thesis, a new approach of the off-resonance waveguiding was introduced, and the phase elements were designed based on this approach. As a proof-of-concept demonstration, a metalens operating in the mid-wave infrared region was shown. The superior performance of the lens was shown by comparing its performance with prominent examples in the literature.

In this thesis, also a novel architecture of metasurface phase elements was proposed. The working principle of this new class was investigated in various configurations. Then, the generality of the proposed architecture was shown, and two metalenses operating in the infrared and visible regions was demonstrated as proof-of-concept. Here, we have obtained significantly improved metasurface performance.

These findings indicate that the proposed metasurface architectures hold great promise for use in optical focusing in the infrared and visible.

Bibliography

- [1] “World's oldest telescope?”, *BBC News*. July 1, 1999.
- [2] D. R. Smith, D. R. Smith, J. B. Pendry, and M. C. K. Wiltshire, “Metamaterials and Negative Refractive Index,” *Science* (80-.), vol. 305, no. 2004, pp. 788–792, 2012.
- [3] C. Della Giovampaola and N. Engheta, “Digital metamaterials,” *Nat. Mater.*, vol. 13, no. 12, pp. 1115–1121, 2014.
- [4] N. Engheta and R. W. Ziolkowski, *Metamaterials: Physics and Engineering Explorations*. Wiley-IEEE Press, 2006.
- [5] W. Cai and V. Shalaev, *Optical Metamaterials: Fundamentals and Applications*. Springer, 2009.
- [6] N. Yu, F. Aieta, P. Genevet, M. A. Kats, and Z. Gaburro, “A broadband, background-free quarter-wave plate based on plasmonic metasurfaces,” *Nano Letters*, vol. 12, pp. 6328–6333, 2012.
- [7] N. Yu and F. Capasso, “Flat optics with designer metasurfaces,” *Nat. Mater.*, vol. 13, no. 2, pp. 139–50, 2014.
- [8] P. Genevet, F. Capasso, F. Aieta, and M. Khorasaninejad, “Recent advances in planar optics: from plasmonic to dielectric metasurfaces,” vol. 4, no. 1, 2017.
- [9] A. Arbabi, Y. Horie, M. Bagheri, and A. Faraon, “Dielectric metasurfaces for complete control of phase and polarization with subwavelength spatial resolution and high transmission,” *Nat. Nanotechnol.*, vol. 10, no. 11, pp. 937–943, 2015.
- [10] A. Arbabi, Y. Horie, A. J. Ball, M. Bagheri, and A. Faraon, “Subwavelength-thick lenses with high numerical apertures and large efficiency based on high-contrast transmitarrays,” *Nat. Commun.*, vol. 6, no. May, pp. 2–7, 2015.
- [11] M. Khorasaninejad, W. T. Chen, R. C. Devlin, J. Oh, A. Y. Zhu, and F. Capasso, “Metalenses at visible wavelengths: Diffraction-limited focusing and subwavelength resolution imaging,” *Science* (80-.), vol. 352, no. 6290, pp. 1190–1194, 2016.
- [12] W. T. Chen, A. Y. Zhu, V. Sanjeev, M. Khorasaninejad, Z. Shi, E. Lee, and F. Capasso, “A broadband achromatic metalens for focusing and imaging in the visible,” *Nat. Nanotechnol.*, vol. 13, no. 3, pp. 220–226, 2018.

- [13] M. Khorasaninejad, A. Y. Zhu, C. Roques-Carmes, W. T. Chen, J. Oh, I. Mishra, R. C. Devlin, and F. Capasso, “Polarization-Insensitive Metalenses at Visible Wavelengths,” *Nano Lett.*, vol. 16, no. 11, pp. 7229–7234, 2016.
- [14] O. Akin and H. V. Demir, “High-efficiency low-crosstalk dielectric metasurfaces of mid-wave infrared focal plane arrays,” *Appl. Phys. Lett.*, vol. 110, no. 14, 2017.
- [15] E. Arbabi, A. Arbabi, S. M. Kamali, Y. Horie, and A. Faraon, “Multiwavelength polarization-insensitive lenses based on dielectric metasurfaces with,” *Optica*, vol. 3, no. 6, pp. 628–633, 2016.
- [16] M. Khorasaninejad, F. Aieta, P. Kanhaiya, M. A. Kats, P. Genevet, D. Rousso, and F. Capasso, “Achromatic Metasurface Lens at Telecommunication Wavelengths,” *Nano Lett.*, vol. 15, no. 8, pp. 5358–5362, 2015.
- [17] S. Wang, P. C. Wu, V. C. Su, Y. C. Lai, M. K. Chen, H. Y. Kuo, B. H. Chen, Y. H. Chen, T. T. Huang, J. H. Wang, R. M. Lin, C. H. Kuan, T. Li, Z. Wang, S. Zhu, and D. P. Tsai, “A broadband achromatic metalens in the visible,” *Nat. Nanotechnol.*, vol. 13, no. 3, pp. 227–232, 2018.
- [18] Z. Zhang, D. Wen, C. Zhang, M. Chen, W. Wang, S. Chen, and X. Chen, “Multifunctional Light Sword Metasurface Lens,” *ACS Photonics*, vol. 5, no. 5, pp. 1794–1799, 2018.
- [19] N. K. Emani, E. Khaidarov, R. Paniagua-Domínguez, Y. H. Fu, V. Valuckas, S. Lu, X. Zhang, S. T. Tan, H. V. Demir, and A. I. Kuznetsov, “High-efficiency and low-loss gallium nitride dielectric metasurfaces for nanophotonics at visible wavelengths,” *Appl. Phys. Lett.*, vol. 111, no. 22, 2017.
- [20] Z. Zhou, J. Li, R. Su, B. Yao, H. Fang, K. Li, L. Zhou, J. Liu, D. Stellinga, C. P. Reardon, T. F. Krauss, and X. Wang, “Efficient Silicon Metasurfaces for Visible Light,” *ACS Photonics*, vol. 4, no. 3, pp. 544–551, 2017.
- [21] O. Akin and H. V. Demir, “Mid-wave infrared metasurface microlensed focal plane array for optical crosstalk suppression,” *Opt. Express*, vol. 23, no. 21, p. 27020, 2015.
- [22] J. Hu, C. H. Liu, X. Ren, L. J. Lauhon, and T. W. Odom, “Plasmonic Lattice Lenses for Multiwavelength Achromatic Focusing,” *ACS Nano*, vol. 10, no. 11, pp. 10275–10282, 2016.
- [23] Y. F. Yu, A. Y. Zhu, R. Paniagua-Domínguez, Y. H. Fu, B. Luk’yanchuk, and A. I.

- Kuznetsov, "High-transmission dielectric metasurface with 2π phase control at visible wavelengths," *Laser Photonics Rev.*, vol. 9, no. 4, pp. 412–418, 2015.
- [24] M. Khorasaninejad, W. Zhu, and K. B. Crozier, "Efficient polarization beam splitter pixels based on a dielectric metasurface," *Optica*, vol. 2, no. 4, p. 376, 2015.
- [25] A. Arbabi, R. M. Briggs, Y. Horie, M. Bagheri, and A. Faraon, "Efficient Dielectric Metasurface Collimating Lenses for Mid-Infrared Quantum Cascade Lasers," vol. 23, no. 26, pp. 33310–33317, 2015.
- [26] M. Khorasaninejad, Z. Shi, A. Y. Zhu, W. T. Chen, V. Sanjeev, A. Zaidi, and F. Capasso, "Achromatic Metalens over 60 nm Bandwidth in the Visible and Metalens with Reverse Chromatic Dispersion," *Nano Lett.*, vol. 17, no. 3, pp. 1819–1824, 2017.
- [27] M. Khorasaninejad and F. Capasso, "Broadband Multifunctional Efficient Meta-Gratings Based on Dielectric Waveguide Phase Shifters," *Nano Lett.*, vol. 15, no. 10, pp. 6709–6715, 2015.
- [28] R. Paniagua-Domínguez, Y. F. Yu, E. Khaidarov, S. Choi, V. Leong, R. M. Bakker, X. Liang, Y. H. Fu, V. Valuckas, L. A. Krivitsky, and A. I. Kuznetsov, "A Metalens with a Near-Unity Numerical Aperture," *Nano Lett.*, vol. 18, no. 3, pp. 2124–2132, 2018.
- [29] S. M. Kamali, E. Arbabi, A. Arbabi, Y. Horie, and A. Faraon, "Highly tunable elastic dielectric metasurface lenses," *Laser Photonics Rev.*, vol. 10, no. 6, pp. 1002–1008, 2016.
- [30] A. Arbabi, E. Arbabi, Y. Horie, S. M. Kamali, S. Han, and A. Faraon, "Aberration Corrected Metasurface Doublet Lens," *CLEO Sci. Innov.*, vol. 1, no. d, pp. 25–26, 2016.
- [31] F. Capasso, "Multiwavelength achromatic metasurfaces by dispersive phase compensation_supple," *Science (80-.)*, vol. 2, no. February, p. science.aaa2494-, 2015.
- [32] C. Ma and Z. Liu, "A super resolution metalens with phase compensation mechanism," *Applied Physics Letters*, vol. 96, no. 18, p. 183103, 2010.
- [33] B. Memarzadeh and H. Mosallaei, "Array of planar plasmonic scatterers functioning as light concentrator," *Optics Letters*, vol. 36, no. 13, pp. 2569-2571, 2011.
- [34] X. Chen, L. Huang, H. Mühlenbernd, G. Li, B. Bai, Q. Tan, G. Jin, C.- W. Qiu, S. Zhang, and T. Zentgraf, "Dual-polarity plasmonic metalens for visible light," *Nature communications*, vol. 3, p. 1198, 2012.

- [35] C. Qu, S. Xiao, S. Sun, Q. He, and L. Zhou, "A theoretical study on the conversion efficiencies of gradient meta-surfaces," *EPL (Europhysics Letters)*, vol. 101, no. 5, p. 54002, 2013.
- [36] C. Pfeiffer and A. Grbic, "Cascaded metasurfaces for complete phase and polarization control," *Applied Physics Letters*, vol. 102, no. 23, p. 231116, 2013.
- [37] M. Pu, P. Chen, Y. Wang, Z. Zhao, C. Huang, C. Wang, X. Ma, and X. Luo, "Anisotropic meta-mirror for achromatic electromagnetic polarization manipulation," *Applied Physics Letters*, vol. 102, no. 13, p. 131906, 2013.
- [38] X. Wan, W. X. Jiang, H. F. Ma, and T. J. Cui, "A broadband transformation optics metasurface lens," *Applied Physics Letters*, vol. 104, no. 15, p. 151601, 2014.
- [39] R. Blanchard, G. Aoust, P. Genevet, N. Yu, M. A. Kats, Z. Gaburro, and F. Capasso, "Modeling nanoscale v-shaped antennas for the design of optically phased arrays," *Physical Review B*, vol. 85, no. 155457, 2012.
- [40] M. Farmahini-Farahani and H. Mosallaei, "Birefringent reflectarray metasurface for beam engineering in infrared," *Optics letters*, vol. 38, no. 4, pp. 462-464, 2013.
- [41] F. Aieta, A. Kabiri, P. Genevet, N. Yu, M. A. Kats, Z. Gaburro, and F. Capasso, "Reflection and refraction of light from metasurfaces with phase discontinuities," *Journal of Nanophotonics*, vol. 6, no. 1, pp. 063532-063532, 2012.
- [42] T. Roy, E. T. Rogers, and N. I. Zheludev, "Sub-wavelength focusing metalens," *Optics express*, vol. 21, no. 6, pp. 7577-7582, 2013.
- [43] L. Huang, X. Chen, H. Mühlenbernd, H. Zhang, S. Chen, B. Bai, Q. Tan, G. Jin, K.-W. Cheah, C.-W. Qiu, et al., "Three-dimensional optical holography using a plasmonic metasurface," *Nature communications*, vol. 4, 2013.
- [44] L. Huang, X. Chen, B. Bai, Q. Tan, G. Jin, T. Zentgraf, and S. Zhang, "Helicity dependent directional surface plasmon polariton excitation using a metasurface with interfacial phase discontinuity," *Light: Science & Applications*, vol. 2, no. 3, p. e70, 2013.
- [45] D. Hu, X. Wang, S. Feng, J. Ye, W. Sun, Q. Kan, P. J. Klar, and Y. Zhang, "Ultrathin terahertz planar elements," *Advanced Optical Materials*, vol. 1, no. 2, pp. 186-191, 2013.
- [46] E. Karimi, S. A. Schulz, I. De Leon, H. Qassim, J. Upham, and R. W. Boyd,

- “Generating optical orbital angular momentum at visible wavelengths using a plasmonic metasurface,” *Light: Science and Applications*, vol. 3, no. 5, p. e167, 2014.
- [47] W. Wang, Z. Guo, R. Li, J. Zhang, Y. Li, Y. Liu, X. Wang, and S. Qu, “Plasmonics metalens independent from the incident polarizations,” *Optics express*, vol. 23, no. 13, pp. 16782-16791, 2015.
- [48] G. Zheng, H. Mühlenbernd, M. Kenney, G. Li, T. Zentgraf, and S. Zhang, “Metasurface holograms reaching 80% efficiency,” *Nature nanotechnology*, vol. 10, no. 4, pp. 308-312, 2015).
- [49] D. Wintz, P. Genevet, A. Ambrosio, A. Woolf, and F. Capasso, “Holographic metalens for switchable focusing of surface plasmons,” *Nano letters*, vol. 15, no. 5, pp. 3585-3589, 2016).
- [50] S. Pancharatnam, “Generalized theory of interference and its applications - Part II. Partially coherent pencils,” *Proc. Indian Acad. Sci. - Sect. A*, vol. 44, no. 6, pp. 398–417, 1956.
- [51] M. V. Berry, “The adiabatic phase and Pancharatnam’s phase for polarized light,” *J. Mod. Opt.*, vol. 34, no. 11, pp. 1401–1407, 1987.
- [52] W. T. Chen, A. Y. Zhu, J. Sisler, Z. Bharwani, and F. Capasso, “A broadband achromatic polarization-insensitive metalens consisting of anisotropic nanostructures,” *Nat. Commun.*, vol. 10, no. 1, pp. 1–7, 2019.
- [53] I. Tanriover and H.V. Demir, “Dielectric Metalens Enabled By Intentional Off-Resonance Waveguiding At Mid-Wave Infrared,” *Appl. Phys. Lett.*, vol. 114,043105, 2019.
- [54] A. Yariv and P. Yeh, *Photonics: Optical Electronics in Modern Communications* (Oxford University Press, New York, NY, 2009), pp. 802–811.
- [55] Edward D. Palik, *Handbook of Optical Constants of Solids Volume 1* (Academic Press, San Diego, CA, 1985) p.547-571.
- [56] M. I. Mishchenko, *J. Quant. Spectrosc. Radiat. Transf.* 100, 268 (2006).
- [57] R. M. Bakker, D. Permyakov, Y. F. Yu, D. Markovich, R. Paniagua-Domínguez, L. Gonzaga, A. Samusev, Y. Kivshar, B. Lukyanchuk, and A. I. Kuznetsov, “Magnetic and electric hotspots with silicon nanodimers,” *Nano Lett.*, vol. 15, no. 3, pp. 2137–2142, 2015.

[58] A. E. Miroshnichenko and Y. S. Kivshar, “Fano resonances in all-dielectric oligomers,” *Nano Lett.*, vol. 12, no. 12, pp. 6459–6463, 2012.